Dear Handling Topic Editor (Yuntao Zhou) and Reviewers:

Re: essd-2026-341

We sincerely appreciate your time and effort in reviewing our manuscript. Your critical comments and insightful suggestions have been invaluable in improving the quality and clarity of our work. We have carefully addressed all the concerns raised during this round of review. In the revised manuscript, all modifications made in response to the reviewers' comments are highlighted in blue for easy identification. Additional experiments, analyses, or clarifications have been incorporated as suggested. The manuscript has been thoroughly proofread to enhance its rigor and readability. Below, we provide point-by-point responses to the reviewers' specific questions. Should further revisions be required, we are committed to addressing them promptly.

Reviewer 2

General assessment

This manuscript presents a global daily sea-surface ageostrophic current dataset for 1993–2023 at 0.25° resolution using a physics-informed dense neural network, AC-PIDNN. The topic is timely and relevant for ESSD. A long-term global dataset that goes beyond purely geostrophic currents could be highly useful for studies of surface transport, eddy energetics, air-sea exchange, and model evaluation.

However, I recommend major revision before publication. The dataset is potentially significant, but the manuscript does not yet provide sufficient evidence that the reconstructed currents represent physically realistic ageostrophic circulation rather than a velocity field constrained to minimize the prescribed momentum residual. The most important issues are the limited independent validation, insufficient discussion of physical assumptions, and incomplete documentation of the dataset and machine-learning workflow.

Q1: Dataset validation is not sufficient for a global ESSD data product

The main validation is based on one TAO mooring location and one ROMS regional simulation. This is not sufficient for a 30-year global dataset. The authors should provide broader independent validation using multiple observational references, such as surface drifters, additional TAO/PIRATA/RAMA moorings, OSCAR or other current products, and regional comparisons in western boundary currents, the Southern Ocean, the tropics, and eastern boundary current systems.

The current validation demonstrates some skill in selected cases, but it does not establish global reliability.

Respond Q1:

We sincerely thank the reviewer for this highly constructive comment. Following the suggestion, we have systematically expanded our validation against 54 in-situ observations from the TAO, PIRATA, and RAMA arrays (https://climatedataguide.ucar.edu/climate-data/tropical-moored-buoy-system-tao-triton-pirata-rama-toga). Besides, the widely used OSCAR dataset was also included in the comparison.

1. Expanded In-situ Validation

As shown in Figure R1(a), these 54 stations are widely distributed across the Pacific (21 stations), Atlantic (14 stations), and Indian Oceans (19 stations). Figure R1(b)–(d) display the Root Mean Square Error (RMSE) of the AC-PIDNN-corrected total currents, OSCAR currents, geostrophic currents (Geo), and Ekman corrected currents (Ekman) against the in-situ measurements. The statistical results are as follows:

- Pacific Ocean: The RMSE of the AC-PIDNN-corrected total current is 0.16 m/s, which outperforms both the Ekman corrected (0.24 m/s) and Geo (0.22 m/s) currents. Furthermore, compared to the standard OSCAR product's error of 0.19 m/s against in-situ data, the AC-PIDNN product reduces the error by approximately 15.8%.
- Indian Ocean: The RMSE of our corrected current is 0.10 m/s, outperforming Ekman corrected (0.13 m/s) and Geo (0.15 m/s) currents. Compared to the OSCAR product's error of 0.13 m/s, the AC-PIDNN product reduces the error by approximately 23.1%.
- Atlantic Ocean: The RMSE of our corrected current is 0.15 m/s, outperforming Ekman corrected (0.22 m/s) and Geo (0.17 m/s) currents. Compared to the OSCAR product's error of 0.17 m/s, the AC-PIDNN product reduces the error by approximately 11.8%.

Meridionally, larger errors are primarily concentrated near the equator (within a latitude band of approximately ±5°). Conversely, accuracy significantly improves in mid-to-low latitudes further away from the equator, aligning much more closely with field observations. Specifically, the RMSE gradually decreases from 0.25 m/s near the equator down to 0.05 m/s in these higher-latitude observation areas.

Overall, across all three major ocean basins, the corrected surface circulations are closer to the in-situ observations compared to the traditional geostrophic and Ekman corrected components, and they consistently demonstrate superior accuracy when compared directly to the OSCAR products.

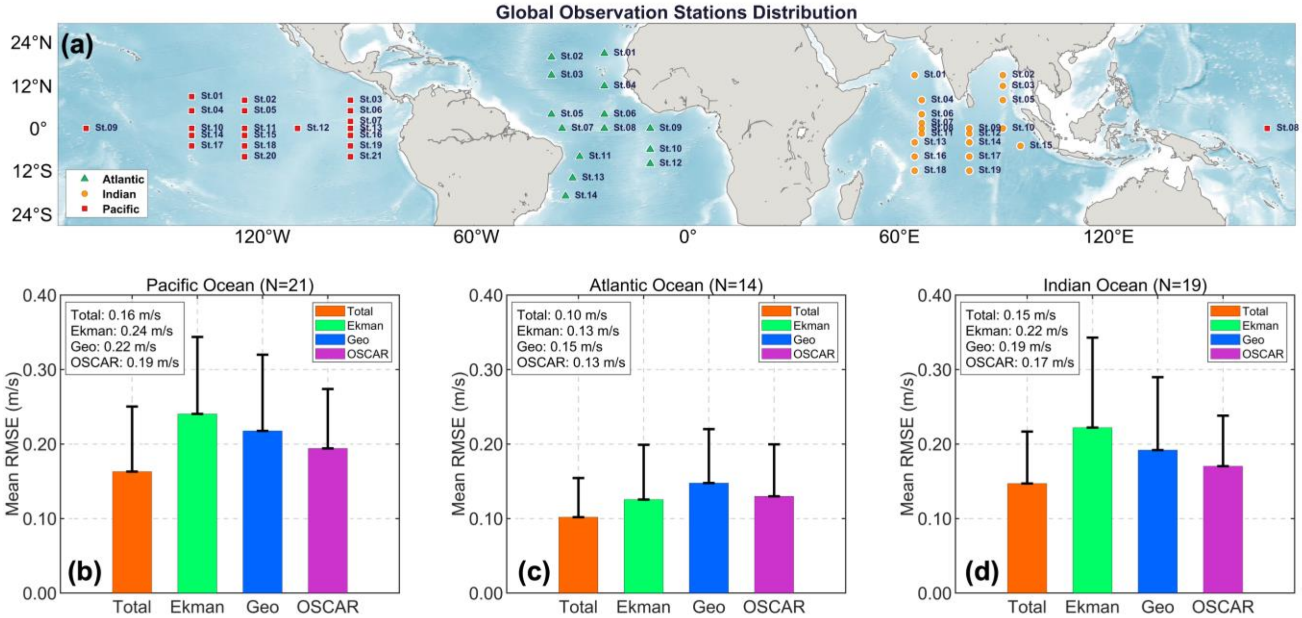

Figure R1. (a) Spatial distribution of TAO/PIRATA/RAMA mooring sites across the Pacific, Atlantic, and Indian Oceans. In-situ observation stations in each ocean basin are individually numbered to facilitate subsequent comparative experiments. (b)–(c) Bar charts illustrating the averaged root-mean-square error (RMSE) between TAO/PIRATA/RAMA mooring observations, OSCAR products and the AC-PIDNN-corrected current fields, geostrophic currents, and Ekman corrected currents for the Pacific, Atlantic, and Indian Oceans, respectively.

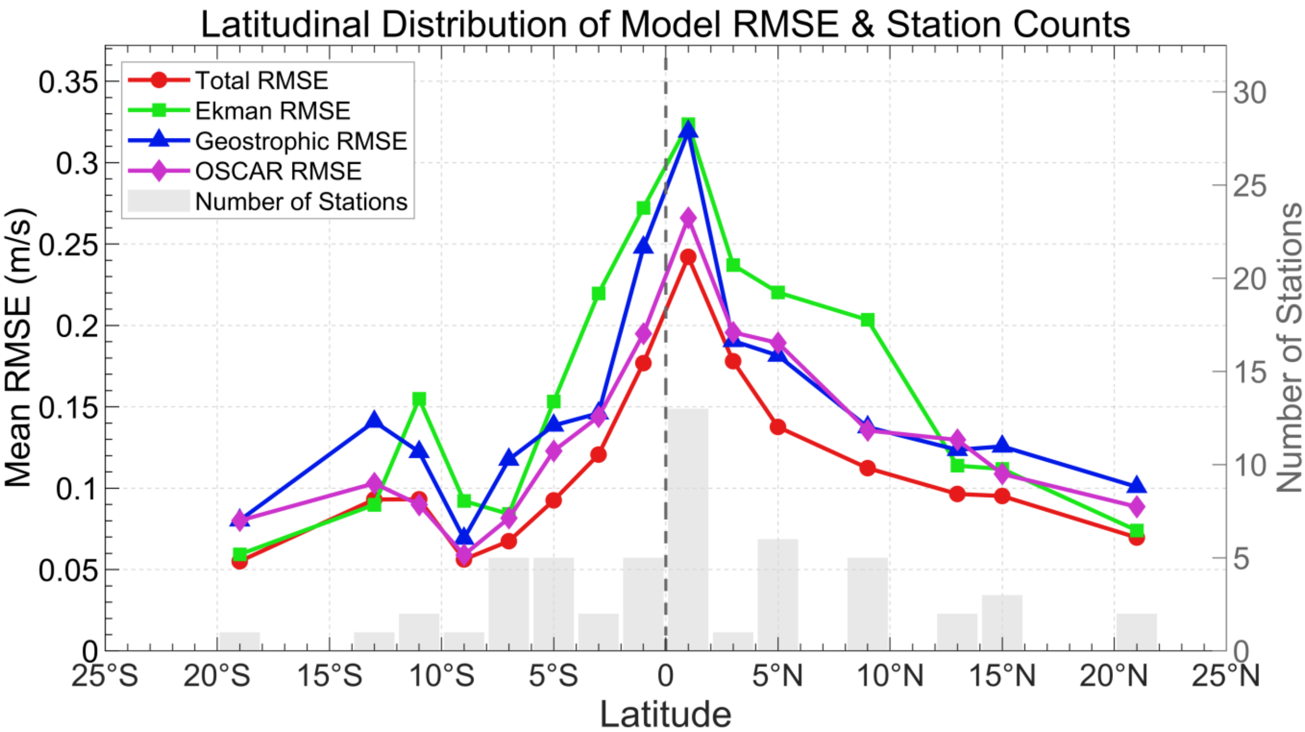

Figure R2 presents the latitudinal error curves of the in-situ measurements against both the corresponding AC-PIDNN-corrected currents and the OSCAR products across the 54 observation stations.

2. Global and Regional Spatial Comparisons (1993–2022 Means)

Besides the comparison with the in-situ mooring observations, we further examined the circulation pattern with the OSCAR. The 30-year mean (1993–2022) total surface flow fields derived from OSCAR with those reconstructed by our method. Overall, the two datasets exhibit similar large-scale circulation patterns. However, because the PIDNN reconstruction additionally accounts for the nonlinear current component, its current magnitudes are generally larger than those in OSCAR and show better agreement with the observations (**Figures R1–R2**). The global mean total velocity for OSCAR is 0.16 m/s, compared to 0.19 m/s for AC-PIDNN.

The differences are particularly pronounced in high-kinetic-energy western boundary current regions, such as the Kuroshio and Gulf Stream, equatorial regions, and Southern Ocean. In these regions, AC-PIDNN more effectively reconstructs the strong currents and intense nonlinear advection characteristics. The incorporation of nonlinear effects also leads to stronger surface divergence in AC-PIDNN than in OSCAR in those regions **as shown in Figure R3**, although the two datasets retain broadly similar large-scale spatial patterns of divergence. The divergence field reconstructed by AC-PIDNN exhibits greater intensity and sharper spatial gradients, particularly in dynamically energetic regions of western boundary current (typical represent by the Kuroshio and Gulf Stream). These differences indicate that AC-PIDNN provides an improved representation of multiscale surface-current dynamics and associated convergence–divergence structures.

All the detailed comparative maps, statistical charts, and discussions mentioned above have been incorporated into **Section 4.1.2** of the revised manuscript and **Supplementary Figure S3**. We thank the reviewer again for this critical suggestion, which has vastly improved the robustness of our validation.

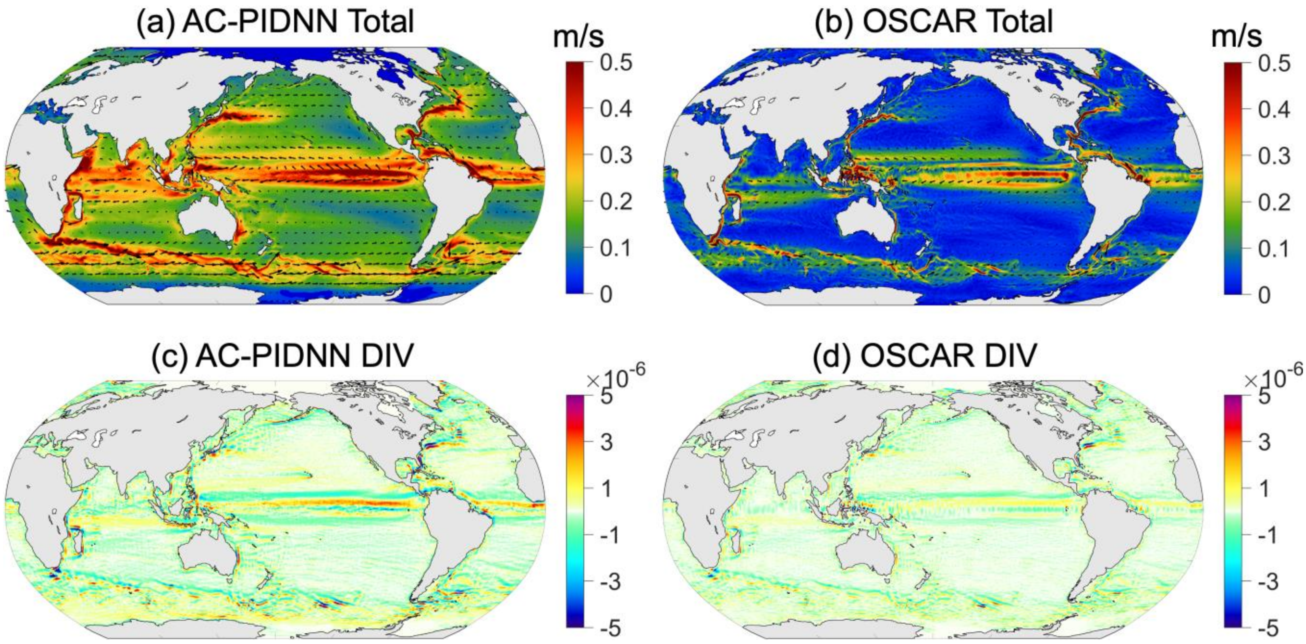

Figure R3. (a) 1993–2022 mean flow field from AC-PIDNN; (b) 1993–2022 mean flow field from the OSCAR product; (c) divergence of the 1993–2022 mean flow field from AC-PIDNN; (d) divergence of the 1993–2022 mean flow field from the OSCAR product

Q2: Momentum residual is not an independent validation metric

The manuscript emphasizes that the reconstructed currents satisfy the imposed momentum balance. However, the momentum residual is part of the training objective. Therefore, a low residual is expected and should not be interpreted as independent evidence that the currents are accurate.

The authors should clearly distinguish between internal consistency with the imposed equations and external validation against independent observations or simulations.

Respond:

We appreciate the reviewer’s professional insight regarding the momentum residual. We agree that the momentum residual is not an "independent external validation" metric, but rather as a rigorous diagnostic criterion for the model's "internal physical consistency." The core rationale of our study is to utilize physical equations to correct the total flow field and isolate the non-linear advection terms. Within this physics-informed inversion framework, maintaining a sufficiently small momentum-equation residual is a prerequisite for the reliable extraction of the nonlinear advection terms. Therefore, while a minimized residual is indeed the result of the training objective converging, it serves as proof that the network has successfully resolved the complex non-linear dynamics.

Following reviewer's concern, in the revised manuscript, we have rigorously distinguished between the concepts of "internal physical consistency" (demonstrated by the momentum residual) and "independent external validation" (demonstrated by comparisons with in-situ observations, as detailed in our previous responses). Furthermore, we have expanded the **Section 3.2.3 of the revised manuscript** to note that incorporating more comprehensive physical mechanisms remains a vital future direction to further bridge the gap between theoretical equation-based reconstructions and real-world measurements.

Q3: The physical problem is underdetermined

The reconstruction attempts to infer total surface currents and ageostrophic components from SSH-derived geostrophic currents, Ekman currents, coordinates, and physical constraints. However, the steady momentum equations do not uniquely determine the ageostrophic current field. Multiple velocity fields may satisfy similar residual constraints.

The authors should discuss uniqueness, regularization, and sensitivity to initialization and loss weighting. This is essential because the dataset is being presented as a physical product, not only as a machine-learning output.

Respond:

We sincerely appreciate this insightful and expert comment. We agree that inverting the total surface current field solely from steady-state momentum equations is fundamentally an underdetermined problem. To ensure that this dataset serves as a physical product rather than merely an output of a deep learning algorithm, we have implemented a multi-layered framework to constrain the solution space, ensure uniqueness, and maintain dynamical consistency.

1. On Uniqueness and the Strong Data Prior

As you correctly noted, underdetermined problems are sensitive to initialization. A random initialization (e.g., Xavier) combined with immediate physics-informed training would likely lead to divergence and cannot guarantee the uniqueness of solutions. This is the primary motivation for our "Three-Stage Training Strategy."

- Stage 1 (Pure Data-Driven Phase): This acts as an explicit "Physical Background Initialization." By forcing the neural network to first anchor to the ocean circulation, we provide a physically consistent starting point.
- Stage 2 (Hybrid Loss Optimization**):** Upon introducing a hybridized loss function that begins blending physical constraints with observational data, we observe a dramatic correction in the flow field's dynamical structure.
- Stage 3 **(**Fully Physics-Constrained Final Output**):** In the final stage, the output is rigorously constrained by the complete physics loss. This proper parameterization forces the reconstructed flow field to obey the fundamental equations of motion.

As demonstrated by the comparison with the observational data and the OSCAR product in the previous response, the solutions align more closely with the actual measurements. The momentum equations do not act as the sole source of information but constrain the model within the subspace defined by observational reality, effectively filtering out non-physical results.

To further demonstrate this, we compare our method with a model using Xavier initialization and direct physics-loss optimization. The comparison clearly shows that without Stage 1, as shown in **Figure R4**, the resulting velocity field is excessively smoothed and deviates significantly from physical reality.

Therefore, our progressive strategy explicitly overcomes the severe sensitivity to initialization inherent in underdetermined problems, ensuring the model converges to a unique oceanographic reality rather than being trapped in a mathematical artifact.

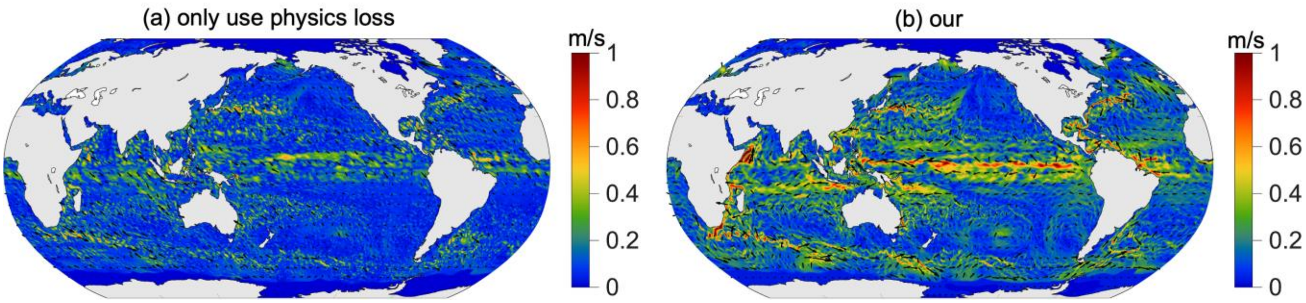

Figure R4 (a) Results of training using only physical loss, (b) Final output of the method in this study.

2. Sensitivity to Loss Weighting and Adaptive Loss Scaling

We recognize that AC-PIDNN models are highly sensitive to the balance between physical and data losses. Static weighting often leads to "gradient pathologies" or overfitting to the steady-state equations. To address this and eliminate the need for manual hyperparameter tuning (e.g., grid search), we implemented an **Adaptive Loss Scaling** mechanism during the Stage 2 hybrid training:

$$\mathcal{L}_{hybrid} = \mathcal{L}_{data} + \lambda \times \mathcal{L}_{physics}$$

where the adaptive weight λ is calculated as $\lambda = \mathrm{sg}\left(\frac{L_{data}}{L_{physics}}\right)$. Here, $\mathrm{sg}(\cdot)$ denotes the stop-gradient operation, ensuring that the weight acts only as a scaling factor and does not interfere with the backpropagation process. This mechanism maintains a 1:1 balance between data and momentum constraints throughout the training, ensuring robustness and reproducibility.

Ultimately, this adaptive scaling mechanism directly addresses your concern regarding loss weighting sensitivity, dynamically harmonizing physical constraints with observational data without relying on arbitrary, trial-and-error hyperparameter tuning.

3. Physical Mapping of Regularization

While we employ L_2 regularization and Dropout to mitigate overfitting, they serve distinct physical roles.

- L_2 Regularization: This is physically analogous to sub-grid scale parameterization and eddy viscosity (*Frederiksen,* 2006). In the context of inverse problems, it suppresses non-physical, high-frequency oscillations in regions of high shear, ensuring the spatial continuity of the divergence and velocity fields (*Smagorinsky*, 1963).
- Dropout: This functions purely as a statistical parameter constraint and lacks a direct fluid-dynamic counterpart, which we have clarified in the revised text.

Consequently, the regularization techniques applied here are not mere mathematical tricks; the L_2 penalty serves an explicit physical purpose by parameterizing sub-grid processes, thereby ensuring the fluid-dynamical stability of the reconstructed currents.

We have integrated these discussions on solution uniqueness, physical initialization, adaptive loss balancing, and the dynamical implications of regularization into the revised **Section 3.2.3 and Supplementary**

Table S1. Thank you once again for your professional guidance in strengthening the physical validity of our work.

Reference

Frederiksen, J. S., & Kepert, S. M. (2006). Dynamical subgrid-scale parameterizations from direct numerical simulations. *Journal of the Atmospheric Sciences*, *63*(11), 3006–3019. https://doi.org/10.1175/jas3795.1

Smagorinsky, J. (1963). General circulation experiments with the primitive equations. *Monthly Weather Review*, *91*(3), 99–164. https://doi.org/10.1175/1520-0493(1963)091<0099:GCEWTP>2.3.CO;2

Q4: Loss function design and training strategy

The novelty of this work lies primarily in the loss function design and the three-stage training strategy rather than in the neural network architecture itself. While the approach is interesting, its implications deserve further discussion.

Stage 1 trains the network using only the data loss, effectively reproducing the geostrophic current field. Stage 2 combines the data and physics losses, allowing the solution to deviate from geostrophy while satisfying the momentum balance. However, Stage 3 removes the data loss entirely and optimizes only the physics loss. Consequently, the final solution is no longer explicitly constrained by the observational prior, but instead by the momentum equations.

This raises two important questions. First, does the final training stage improve agreement with independent observations, or does it primarily reduce the momentum residual? Second, does minimizing the physics loss alone lead to a unique and physically meaningful reconstruction?

A simple ablation experiment (as suggested by Reviewer #1) comparing the outputs after Stages 1, 2, and 3 against independent observations would help quantify the contribution of each training stage and clarify the balance between observational fidelity and dynamical consistency.

Respond Q4:

We sincerely thank the reviewer for this insightful comment. To address two critical questions, we have detailed the rationale behind our approach and conducted the suggested ablation experiment.

1. Rationale of the Three-Stage Training Strategy

Since training deep learning models solely on physical equations has the risk of converging to non-unique, trivial solutions or overly smoothed fields, we mitigate this by gradually shifting the optimization landscape from a data-driven initialization to a strictly physics-constrained refinement. The loss functions are defined as follows:

$$\mathcal{L}_{data} = \frac{1}{N}\sum_{i=1}^{N}(\|u_{Pseudo\ labels} - u_i\|^2 + \|v_{Pseudo\ labels} - v_i\|^2)$$

$$\mathcal{L}_{physics} = \frac{1}{N}\sum_{i=1}^{N}\left(\|ADV_x + COR_x + PGF_x + WIND_x\|^2 + \left\|ADV_y + COR_y + PGF_y + WIND_y\right\|^2\right)$$

$$\mathcal{L}_{hybrid} = \mathcal{L}_{data} + sg\left(\frac{\mathcal{L}_{data}}{\mathcal{L}_{physics}}\right) \times \mathcal{L}_{physics}$$

Where the operator sg(·) denotes a stop-gradient operation ensuring that $\mathrm{sg}\left(\frac{\mathcal{L}_{data}}{\mathcal{L}_{physics}}\right)$ acts strictly as a numerical scaling factor rather than a differentiable variable, $(u_{Pseudo\ labels}, v_{Pseudo\ labels})$ represents the pseudo-labels for model initialization, which are constructed using the sum of the corresponding geostrophic and Ekman components. The training is systematically executed in three stages:

- **Stage 1 (Data-Driven Initialization):** Using only $\mathcal{L}_{data}$ (Learning rate = 0.001, Epochs = 1000). This allows the model to rapidly capture the features of the geostrophic and Ekman corrected flows. It establishes a physically reasonable starting point, preventing the non-uniqueness problem that occurs when starting from random initialization, as shown in **Figure R4 (Q3)**.

- **Stage 2 (Transitional Hybrid Optimization):** Using $\mathcal{L}_{hybrid}$ (Learning rate = 0.0001, Epochs = 1000). Enforcing strong physical constraints too abruptly can cause gradient instability. This hybrid stage acts as a buffer, gently introducing momentum balance constraints to guide the model away from purely data-fitted local minima.

- **Stage 3 (Pure Physics Refinement):** Using only $\mathcal{L}_{physics}$ (Learning rate = 0.00001, Epochs = 10000). By removing the data constraint, we allow the network to minimize the momentum residuals strictly.

Because the model is already anchored in a realistic state by Stages 1 and 2, minimizing $\mathcal{L}_{physics}$ does not lead to an arbitrary solution; instead, it accurately resolves the non-linear dynamical components that cannot be captured by data fitting alone.

Ultimately, this progressive training design addressed your concern: by systematically securing observational fidelity in the early stages, the optimization of the physics loss alone in Stage 3 acts as a final dynamical polishing. As proved by the comparison with only trained on the physics loss in our previous response, this guarantees a unique, physically meaningful reconstruction.

2. Ablation Experiment: Observational Fidelity (Figure R6) vs. Dynamical Consistency (Figure R5)

To answer your question regarding whether Stage 3 improves agreement with independent observations or merely reduces momentum residuals, we conducted a quantitative ablation experiment using 2021 flow field data. We saved the output of Stage 1, Stage 2 and Stage 3 to compare against the in-suit observation.

(1) Dynamical Consistency

Figures R9(a)–(c) illustrate the annual mean surface current fields generated by the AC-PIDNN model during Stages 1, 2, and 3, respectively. Correspondingly, Figures R9(d)–(f) map the momentum balance residual (Bal) for these three stages. The progression reveals a stark contrast in dynamical consistency.

- **Stage 1 (Data-Loss Only Baseline):** Because this initial stage relies exclusively on $Loss_{data}$ without any embedded physical constraints, the neural network acts as a standard data-fitting algorithm. Consequently, the output entirely lacks momentum balance correction, leading to severe dynamical inconsistencies where the momentum residuals exceed **100%** across the vast majority of the global ocean regions, as shown in Figure R9 (a) and (d).
- **Stage 2 (Hybrid Loss Optimization):** Upon introducing a hybridized loss function that begins blending physical constraints with observational data, we observe a dramatic correction in the flow field's dynamical structure. The global mean momentum residual drops precipitously to approximately **51%**, as shown in Figure R9 (b and (e).
- **Stage 3 (Fully Physics-Constrained Final Output):** In the final stage, the output is rigorously constrained by the complete physics loss. This proper parameterization forces the reconstructed flow

field to obey the fundamental equations of motion, vastly improving the momentum balance and reducing the global average momentum residual to a mere **1.2%**, as shown in Figure R9 (c) and (f).

Therefore, this progression proves that Stage 3 does not merely reduce numerical errors, but fundamentally ensures the physical realism of the reconstructed currents by driving momentum residuals to negligible levels.

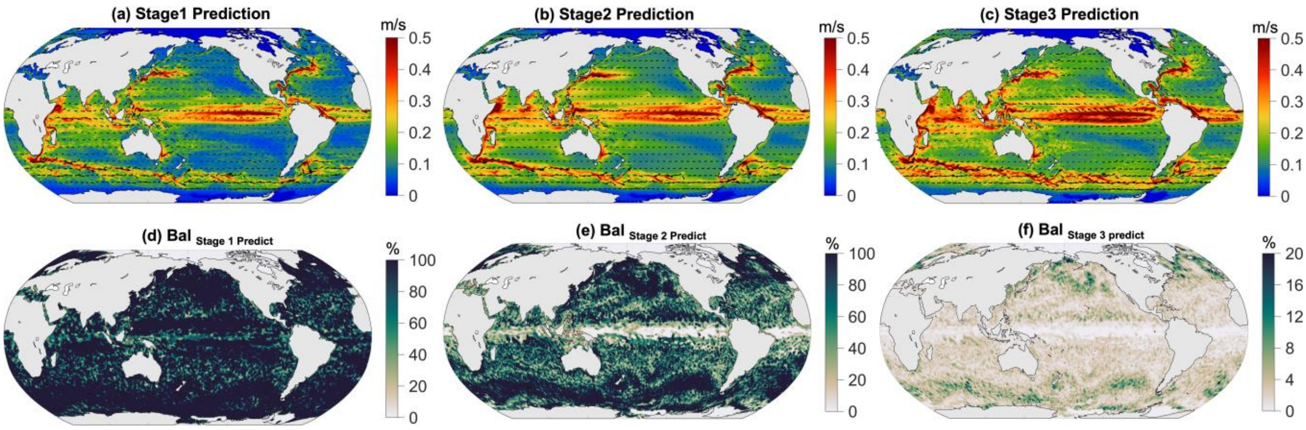

Figure R5. (a) Mean output current field of AC-PIDNN Stage 1 in 2021; (b) Mean output current field of AC-PIDNN Stage 2 in 2021; (c) Final mean output current field of AC-PIDNN Stage 3 in 2021; (d) Momentum balance (Bal) results for Stage 1; (e) Momentum balance (Bal) results for Stage 2; (f) Momentum balance (Bal) results for Stage 3.

(2) Observational Fidelity

To confirm that this improved dynamical balance translates to real-world accuracy, we further evaluated the outputs of all three training stages, as well as the standard OSCAR product, against independent in-situ mooring data. Due to the incomplete coverage of the 2022 OSCAR dataset and computational time constraints during training, our comparative analysis focused on the velocity time series from successfully matched observation stations in 2021, as illustrated in Figure R8. As expected, the progressive incorporation of physical laws systematically refines the accuracy of the modeled velocities:

- **Stage 1 Average Error:** 0.17 m/s
- **Stage 2 Average Error:** 0.16 m/s

- **Stage 3 Average Error:** 0.13 m/s
- **OSCAR Product Average Error:** 0.17 m/s

The data clearly shows that the Stage 3 output aligns most closely with the in-situ measurements, significantly outperforming the Stage 1 baseline, the intermediate Stage 2 output, and the widely used OSCAR product. Purely data-driven approaches (Stage 1) are highly susceptible to the inherent noise and spatial gaps present in multi-source satellite altimetry and scatterometry data. By enforcing momentum conservation, the subsequent physics-informed stages effectively filter out dynamically impossible artifacts, preventing overfitting to observational noise and yielding a flow field that is both physically coherent and statistically more accurate.

This comparison with station-based observational errors firmly substantiates the superiority and absolute necessity of the physics-informed training stages. In conclusion, these results directly address your concern: the physical constraints applied in Stage 3 do not merely perform a mathematical reduction of momentum residuals, but genuinely enhance the model's predictive skill against independent, real-world observations.

We have incorporated the comprehensive results of this ablation experiment, alongside the associated figures and an expanded dynamical discussion, into the **Supplementary Material (Figure S1 to Figure S2)** of the revised manuscript. We once again thank you for your valuable and constructive comments.

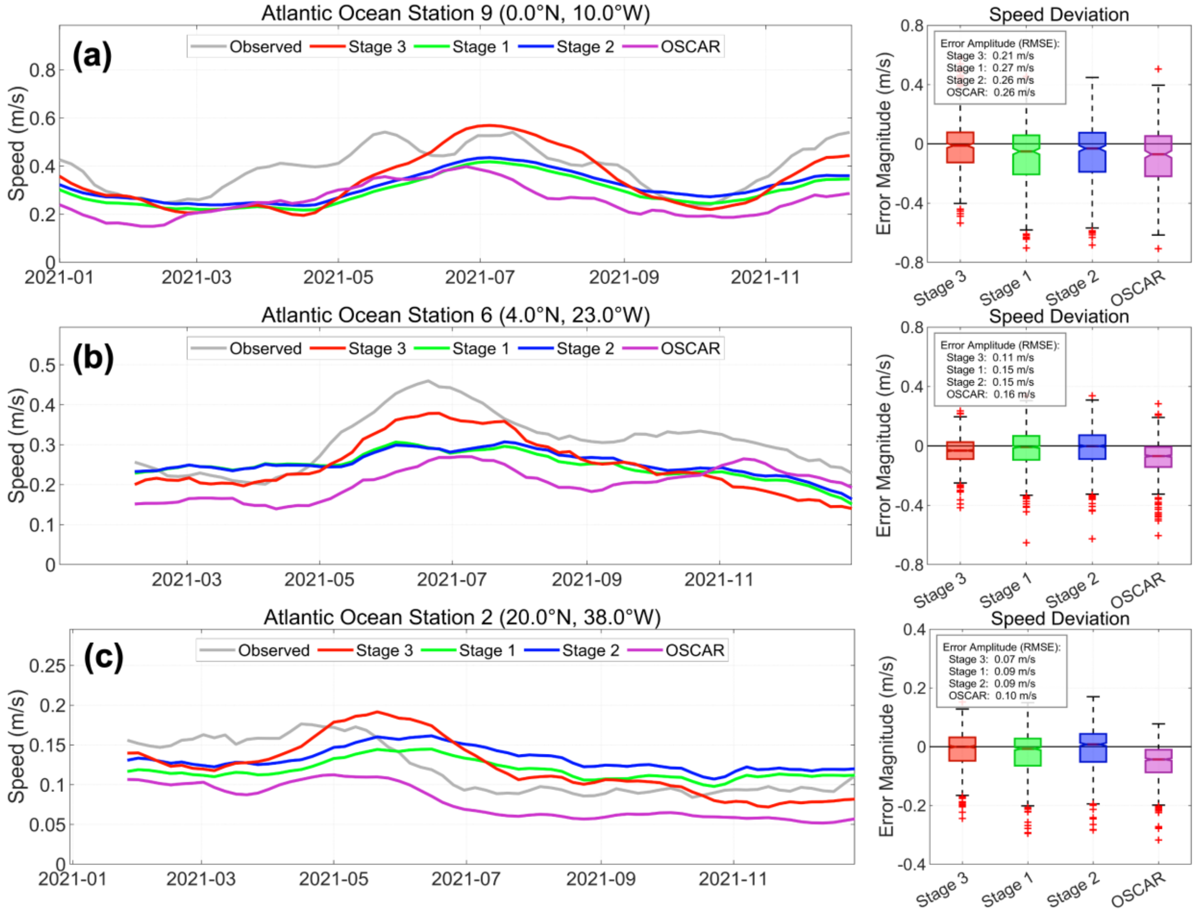

Figure R6. Comparison of the output current fields from the three training stages of AC-PIDNN and OSCAR product velocities against in-situ observational data.

Daily Global Sea Surface Ageostrophic Current Dataset from 1993–2023 via Physics-Informed Deep Learning

Guangxi Cui[1,2], Ka-Veng Yuen[3], Ying Chen[1,2], Zhiqiang Liu[4], Dingqi Yang[5], Guanliang Liu[6,7], Zhongya Cai[1,2*]

[1]State Key Laboratory of Internet of Things for Smart City, Department of Ocean Science and Technology, University of Macau

[2]Center for Ocean Research in Hong Kong and Macau (CORE), Hong Kong

[3]State Key Laboratory of Internet of Things for Smart City, Department of Civil and Environmental Engineering, University of Macau

[4]Department of Ocean Science and Engineering and Center for Complex Flows and Soft Matter Research, Southern University of Science and Technology, Shenzhen, China

[5]State Key Laboratory of Internet of Things for Smart City, Department of Computer and Information Science, University of Macau

[6]State Key Laboratory of Physical Oceanography, Institute of Oceanographic Instrumentation, Shandong Academy of Sciences

[7]Qilu University of Technology (Shandong Academy of Sciences), Jinan

Correspondence to: Zhongya Cai (zycai@edu.mo)

Abstract

Surface ocean circulation shapes climate, air-sea exchange, and the transport of heat, carbon, and other tracers, yet most long-term global datasets rely primarily on geostrophic balance and therefore miss important ageostrophic motions. Here, we reconstruct global daily sea surface circulation at 0.25° resolution from 1993 to 2023 using a physics-informed framework that integrates satellite altimetry with momentum constraints from geostrophic balance, wind stress, and nonlinear advection. The resulting dataset is dynamically consistent, with a mean momentum-balance error below 1.5%, and reduces the median velocity error against independent mooring observations to 0.10 m s^{-1}, compared with 0.20 m s^{-1} for geostrophic currents and 0.18 m s^{-1} for Ekman-corrected currents. We show that geostrophic flow sets the large-scale circulation, whereas Ekman and nonlinear contributions are smaller but comparable in magnitude to each other. Although nonlinear advection contributes little to relative vorticity, it strongly shapes surface divergence and the fine-scale structure of eddy kinetic energy. Our results show that nonlinear ageostrophic flow is an essential component of global surface circulation and that neglecting it limits our ability to resolve surface transport and variability on climatically relevant scales.

Index Term: Ageostrophic Circulation, Ekman Dynamics, Physics-Informed Dense Neural Network, Satellite Altimetry

1 Introduction

Surface ocean circulation regulates climate, air-sea exchange, and the transport of heat, carbon, nutrients, and other tracers. Over the past several decades, satellite remote sensing has provided the principal observational basis for studying upper-ocean circulation (Du et al., 2021; Fan et al., 2025; Shang et al., 2025). Geostrophic currents derived from sea surface height have become central to analyses of ocean dynamics (Xie et al., 2024), climate change, and ecosystem assessments (Timmermans and Marshall, 2020; Srinivasan and Tsontos, 2023). However, geostrophic currents neglect the influence of ageostrophic processes, such as wind stress and nonlinear effects (Hiron et al., 2021). Although ageostrophic processes are relatively small in magnitude, both observational data and numerical simulations have consistently shown that they substantially modulate ocean circulation (Rio et al., 2014; Edwards et al., 2024). Ageostrophic motions play a crucial role in the evolution and adjustment of ocean circulation. For example, nonlinear effects contribute to the evolution of mesoscale eddies (Li et al., 2022) and are important for the transport of heat, dissolved carbon, and tracers (Ueno et al., 2023). Studies have also shown that nonlinear processes can reduce geostrophic current speeds by more than 0.2 m s^{-1} (Cao et al., 2023b), whereas wind-driven Ekman effects can enhance sea surface current velocities (Rio et al., 2014). Neglecting ageostrophic processes (Armitage et al., 2017; Shankar et al., 2002; Cho et al., 2025) omits the complex features introduced by variations in nonlinear forcing and wind stress (Andres et al., 2008; Buckingham et al., 2021), leading to substantial discrepancies with drifter-observed velocities (Douglass and Richman, 2015; Uchida and Imawaki, 2003). This omission introduces uncertainties in understanding the long-term evolution and energy transformation of ocean circulation.

The influence of ageostrophic motions is especially pronounced in energetically active regions such as western boundary currents, the subtropical countercurrent, and the Antarctic Circumpolar Current, where their kinetic energy can be comparable to that of geostrophic motions (Zhang et al., 2019). The development of ageostrophic motions can disrupt geostrophic balance, promote forward energy transfer, and influence the inverse transfer of geostrophic energy, leading to an increase in the mean geostrophic wavenumber (Kafiabad et al., 2019; Thomas and Daniel, 2021). Ageostrophic motions are also closely linked to marine ecosystems: the intense vertical motions they induce provide an important pathway for delivering nutrients into the euphotic zone and thereby help regulate primary productivity and carbon sequestration in the global ocean (Aluie et al., 2018; Liu et al., 2025; Masuda et al., 2021).

Most existing corrections to sea surface circulation adopt a steady-state framework (Fraser et al., 2024), and two main methods are commonly used to represent nonlinear effects. One assumes axisymmetric vortices and reduces nonlinear forcing to the centrifugal term in the gradient wind equation (Ioannou et al., 2019). The other uses a perturbation expansion in which the nonlinear term is approximated by the rate of change of geostrophic velocity (Penven et al., 2014). In practice, most previous studies have used iterative schemes for circulation correction (Cao et al., 2023a; Penven et al., 2014). The iterative solution of the gradient wind equation was first developed in atmospheric science (Cao et al., 2023a; Penven et al., 2014) and later introduced into oceanography. Such schemes have been applied to a large gyre in the Mozambique Channel, mesoscale eddies in the Mediterranean Sea (Cao et al., 2023a; Penven et al., 2014; Morales-Márquez et al., 2023), and the correction of the global sea surface circulation field (Cao et al., 2023b; Ruiz et al., 2014). However, these schemes can diverge when the gradient wind equation has no solution (Douglass and Richman, 2015; Qiu et al., 2019). Furthermore, the stopping criterion for these schemes is typically when the velocity residual either begins to diverge or decreases below a predefined threshold (Douglass and Richman, 2015; Qiu et al., 2019), which is commonly set to 0.01 m s^{-1} in the literature (Cao et al., 2023a; Arnason et al., 1962; Penven et al., 2014). As a result, the dynamical consistency of the corrected solution remains uncertain.

Recent advances in artificial intelligence (AI) have created new opportunities for oceanographic data analysis and reconstruction (Li et al., 2020; Dong et al., 2022; Qin et al., 2023; Cui et al., 2025). AI has been applied to infer ocean surface dynamic parameters and structures (Bonino et al., 2024; Jang et al., 2022; Lenain et al., 2026; Cui et al., 2026), such as subsurface eddy kinetic energy (Xie et al., 2024), subsurface thermohaline structure (Zhou et al., 2024), and sea surface temperature (Bonino et al., 2024; Kumar et al., 2021; Kartal, 2023). AI-based research on sea surface circulation is also beginning to emerge. Existing work primarily uses machine learning to replace traditional geostrophic relationships by combining satellite-observed variables, such as sea surface height, sea surface temperature, and wind stress, to reconstruct global sea surface circulation fields (Sinha and Abernathey, 2021; Manucharyan et al., 2021). However, these approaches do not fully integrate the governing physical equations of ocean surface circulation into the learning framework for ageostrophic correction. As a result, the reconstructed flow fields can retain non-negligible dynamical imbalances, as reflected in residual terms of the momentum equations.

Here, we develop a physics-informed dense neural network with ageostrophic circulation correction (AC-PIDNN) to reconstruct global sea surface circulation while explicitly enforcing momentum balance. The model integrates constraints from geostrophic balance, wind stress, and nonlinear advection to recover ageostrophic flow from satellite-observed sea surface height gradients. Using the AC-PIDNN, we generate a daily global ageostrophic current dataset from 1993 to 2023 at a spatial resolution of 0.25°. This framework enables a dynamically consistent assessment of how ageostrophic processes shape global surface circulation, divergence, and eddy energetics. The structure of this paper is as follows: Section 2 describes the data used; Section 3 introduces the proposed methodology; Section 4 presents the experimental results and discussions; Sections 5 and 6 present the code and data availability and conclusions, respectively.

2 Data

2.1 Satellite Data

The dataset used in this study includes the daily Absolute Dynamic Topography (ADT) gridded data, geostrophic currents $\vec{V}_{geo} =(u_{geo}, v_{geo})$, and the corresponding surface Ekman components of the global ocean, which were downloaded from https://data.marine.copernicus.eu/product. The ADT gridded data are provided by the French Space Agency (CNES) through the Archiving, Validation, and Interpretation of Satellite Oceanographic data (AVISO) service, and are processed by the CNES/CLS Data Unification and Altimeter Combination System (DUACS). This system integrates observations from all

Sentinel altimetry missions as well as other collaborative or opportunistic missions. The datasets incorporate high-quality altimeter measurements and geophysical corrections and are generated using a consistent correction system to ensure maximum data quality and to minimize temporal artifacts. This dataset also provides geostrophic current $\vec{V}_{geo}$ based on the geostrophic balance. These data used in this study have a temporal resolution of 1 day and a spatial resolution of 1/4°.

The surface Ekman components are obtained from the global Copernicus Ocean (GLOBCURRENT) surface and 15-meter Ekman and geostrophic current datasets. These data are derived by applying an empirical Ekman model to ERA5 wind stress fields (Mulet et al., 2021; Rio et al., 2014), with the calculation taking into account both wind stress and the mixed layer depth. The inclusion of mixed layer depth reflects the dynamic variability of Ekman depth across time and space. This product provides datasets on a 1/4° regular grid, offering current velocity fields at the surface and at 15 m depth with hourly, daily, and monthly temporal resolutions.

2.2 Simulation Data

To validate the performance of the method proposed in this study, we conducted a high-resolution numerical simulation using the Regional Ocean Modeling System (ROMS) (Shchepetkin and Mcwilliams, 2005). The simulation results served as the “ground truth” for assessing the accuracy of our approach. ROMS is a widely used, high-resolution numerical framework designed for simulating regional-scale oceanic and atmospheric processes. By solving the governing equations of fluid motion, ROMS provides accurate simulations of ocean circulation, temperature, salinity, and other essential physical properties while maintaining strong dynamical consistency and numerical stability. In this study, the simulation configuration covers the western Pacific region (5°N–32°N, 109°E–141°E) with a spatial resolution of 3 km. The output is provided as a 30-day mean field. This high-resolution setup effectively resolves mesoscale and submesoscale oceanic dynamical processes, thereby establishing a reliable and physically consistent numerical benchmark for evaluating the accuracy and effectiveness of our method. It also forms a foundation for further investigation of regional circulation characteristics and underlying dynamical mechanisms.

3 Methodology

3.1 The Steady State Momentum Balance Equations

In this study, the surface sea currents within the Ekman layer are assumed satisfy the steady state momentum balance between nonlinear advection, pressure gradient force, Coriolis force and wind stress (Sudre et al., 2013; Van Meurs and Niiler, 1997):

$$\overbrace{u\frac{\partial u}{\partial x}+v\frac{\partial u}{\partial y}}^{ADV_x} = \overbrace{fv}^{COR_x} \overbrace{-g\frac{\partial \eta}{\partial x}}^{PGF_x} + \overbrace{\frac{1}{h_e}\left(\frac{\tau_x}{\rho}-r_e u_{ekman}\right)}^{WIND_x} \tag{1}$$

$$\overbrace{u\frac{\partial v}{\partial x}+v\frac{\partial v}{\partial y}}^{ADV_y}=\overbrace{-fu}^{COR_y}\overbrace{-g\frac{\partial \eta}{\partial y}}^{PGF_y}+\overbrace{\frac{1}{h_e}\left(\frac{\tau_y}{\rho}-r_e v_{ekman}\right)}^{WIND_y} \tag{2}$$

where, u and v are the zonal and meridional velocities; η is the sea surface height from ADT data; f represents the Coriolis force parameter; g is gravity acceleration; and $\tau(\tau_x, \tau_y)$ is the wind stress field. The h_e and r_e are thickness of the Ekman layer and the linear drag coefficient that represents the vertical viscosity terms as a body force on the Ekman components. With the information from the locally estimated h_e and r_e, the $\vec{V}_{ekman} = (u_{ekamn}, v_{ekamn})$, can be calculated based on the wind stress field. In our calculation, the $\overbrace{\frac{1}{h_e}(\frac{\tau_x}{\rho} - r_e u_{ekman})}^{WIND_x}$ and $\overbrace{\frac{1}{h_e}(\frac{\tau_y}{\rho} - r_e v_{ekman})}^{WIND_y}$ are represented by the $-f v_{ekman}$ and $f u_{ekman}$, in which u_{ekman} and v_{ekman} are the Ekman component of current in GLOBCURRENT data to simplify the calculation.

3.2 Physics-informed Density Neural Networks for Correcting Ageostrophic Current (AC-PIDNN)

In this study, we propose a physics-informed neural network (PINN)–based architecture for correcting ageostrophic current, termed AC-PIDNN. The overall structure, as shown in Figure 1, consists of four components: input module, custom density neural networks module, and loss function module.

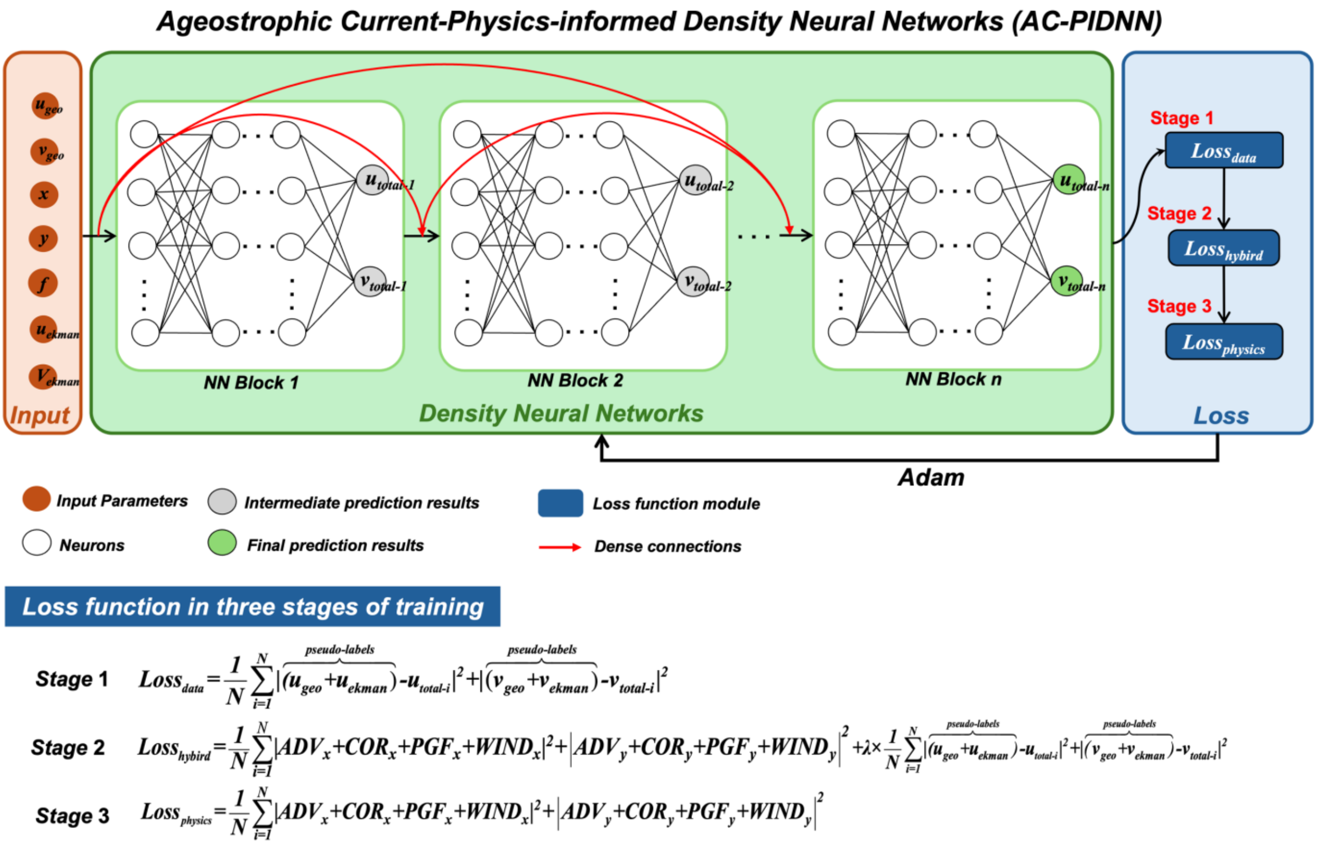

Figure 1: Schematic diagram of the proposed sea surface circulation correction model (AC-PIDNN).

3.2.1 Input Module

The model inputs include geostrophic current components derived from the geostrophic approximation (u_{geo},v_{geo}), surface Ekman current components (u_{ekman}, v_{ekman}), Coriolis parameter f, and geographical coordinates (x, y). The input features be represented as:

$$\mathbf{X} = [u_{geo}, v_{geo}, x, y, f, u_{ekman}, v_{ekman}] \tag{3}$$

The geostrophic currents are calculated based on the geostrophic balance:

$$f v_{geo} - g\frac{\partial \eta}{\partial x} = 0 \tag{4}$$

$$-f u_{geo} - g\frac{\partial \eta}{\partial y} = 0 \tag{5}$$

In this study, u_{geo} and v_{geo} are directly derived from the AVISO dataset. However, Equations (4) and (5) become singular at the equator ($f = 0$), and they are also problematic in its vicinity due to the weak Coriolis effect. To address this issue, within the latitude band of ±2°, this study adopts the so-called *"semi-geostrophic"* approximation to compute the equatorial current components $\vec{V}_{sg} = (u_{sg}, v_{sg})$, which replace the geostrophic currents in this region (Sudre et al., 2013):

$$u_{sg} = -\frac{g}{\beta}\frac{\partial^2 \eta}{\partial y^2} \tag{6}$$

$$v_{sg} = \frac{g}{\beta}\frac{\partial^2 \eta}{\partial x^2} \tag{7}$$

where β is the meridional gradient of the Coriolis parameter, defined as $\beta = \frac{2\Omega cos\varphi}{R}$, Ω is the Earth's angular velocity of rotation, φ is the latitude, R is the Earth's radius.

3.2.2 Density Neural Networks Module

The Density Neural Networks module incorporates multiple fully connected neural network (NN) layers, organized into NN submodules, and employs residual connections similar to ResNet (Razavi et al., 2024) to facilitate efficient information transfer between modules. This design aims to minimize the loss of information from the initial geostrophic current field during feature extraction and to accelerate model convergence and enhance stability. The AC-PIDNN architecture employs three NN blocks, each containing five hidden layers with 100 neurons per layer. Each NN block consists of a sequence of fully connected transformations:

$$h^{(l)} = \sigma\left(W^{(l)}h^{(l-1)} + b^{(l)}\right),\ l = 1, \dots, L \tag{8}$$

where $\boldsymbol{h}^{(0)} = \mathbf{X}, W^{(l)}$ and $b^{(l)}$ are the trainable weights and biases of the l -th layer,$\sigma(\cdot)$ denotes the activation function, and L is the number of hidden layers in each block. To preserve the physical meaning of the geostrophic input and reduce the loss of dynamical information, a residual connection is applied:

$$h^{(l)} = f(h^{(l)}) + h^{(l-1)} \tag{9}$$

This residual mechanism allows the NN block to learn corrections to the geostrophic current field rather than re-learning it from scratch. From a physical perspective, the predicted current field $\vec{V}_{total} = (u_{total}, v_{total})$ can be expressed as the sum of the geostrophic component and a correction term:

$$u_{total} = u_{geo} + \Delta u(\mathbf{X}; \theta) \tag{10}$$

$$v_{total} = v_{geo} + \Delta v(\mathbf{X}; \theta) \tag{11}$$

where Δu and Δv are the data-driven corrections parameterized by the network weights θ. This formulation ensures that the essential dynamical information from the geostrophic approximation is retained while enabling the network to learn the ageostrophic corrections. Consequently, the residual structure accelerates convergence, improves gradient stability during backpropagation, and prevents the model from overfitting to spurious patterns in the training data.

3.2.3 Loss Function Module and Training Strategy

The loss function module consists of three customized loss functions. To address this and eliminate the need for manual hyperparameter tuning (e.g., grid search), we implemented an adaptive loss scaling mechanism during the Stage 2 hybrid training.

$$Loss_{data} = \frac{1}{N}\sum_{i=1}^{N}\|u_{Pseudo\ labels} - u_{total-i}\|^2 + \|v_{Pseudo\ labels} - v_{total-i}\|^2 \quad (12)$$

$$Loss_{physics} = \frac{1}{N}\sum_{i=1}^{N}\|ADV_x + COR_x + PGF_x + WIND_x\|^2 + \|ADV_y + COR_y + PGF_y + WIND_y\|^2 \quad (13)$$

$$Loss_{hybird} = Loss_{data} + \lambda \times Loss_{physics} \quad (14)$$

Here, N denotes the number of training samples; $\vec{V}_{Pseudo\ labels} = (u_{Pseudo\ labels}, v_{Pseudo\ labels})$ represents the pseudo-labels for model initialization, which are constructed using the sum of the corresponding geostrophic and Ekman components; and $\vec{V}_{total-i} = (u_{total-i}, v_{total-i})$ are the model-predicted current components in the $i-th$ epoch; $Loss_{data}$ represents the mean squared error between the predicted and geostrophic currents, and is used for initial model fitting; $Loss_{physics}$ measures the residuals of the predicted current field in the momentum equations, constraining the outputs to satisfy the two-dimensional momentum balance as closely as possible; It is worth noting that the $Loss_{physics}$ is calculated for each predicted $(u_{total-i}, v_{total-i})$, which is a dynamic value. $Loss_{hybird}$ is a weighted combination of the above two, enabling a smooth transition from data-driven to physics-driven learning by gradually increasing the weight of physical constraints during training. The adaptive weight λ is calculated as $\lambda = \mathrm{sg}\left(\frac{L_{data}}{L_{physics}}\right)$. Here, $\mathrm{sg}(\cdot)$ denotes the stop-gradient operation, ensuring that the weight acts only as a scaling factor and does not interfere with the backpropagation process. This mechanism maintains a 1:1 balance between data and momentum constraints throughout the training, ensuring robustness and reproducibility.

The adaptive optimization algorithm Adam (Kingma and Ba, 2014) is employed to minimize the loss function, and neural network parameters are initialized using the Xavier scheme (Glorot and Bengio, 2010). The hyperbolic tangent ($\tanh$) is adopted as the activation function. Furthermore, L_2 regularization and dropout are utilized to mitigate overfitting, with each serving distinct physical roles within the architecture. Once training converges and the loss function reaches a sufficiently small value, the predicted (u_{total}, v_{total}) values approximate the solutions of the momentum equations (1) and (2). To ensure stability and accuracy, a three-stage training strategy is adopted:

Stage 1 (Data-Driven Initialization): Using only $Loss_{data}$ (Learning rate = 0.001, Epochs = 1000). This allows the model to rapidly capture the macroscopic features of the geostrophic and Ekman flows. It establishes a physically reasonable starting point, preventing the non-uniqueness problem that occurs when starting from random initialization.

Stage 2 (Transitional Hybrid Optimization): Using $Loss_{hybird}$ (Learning rate = 0.0001, Epochs = 1000). Enforcing strong physical constraints too abruptly can cause gradient instability. This hybrid stage acts as a buffer, gently introducing momentum balance constraints to guide the model away from purely data-fitted local minima.

Stage 3 (Pure Physics Refinement): Using only $Loss_{physics}$ (Learning rate = 0.00001, Epochs = 10000). By removing the data constraint, we allow the network to minimize the momentum residuals strictly. Because the model is already anchored in a realistic state by Stages 1 and 2, minimizing $Loss_{physics}$ does not lead to an arbitrary solution; instead, it accurately isolates and resolves the non-linear dynamical components that cannot be captured by data fitting alone.

Notably, to successfully isolate the ageostrophic components from the momentum equations, the combined geostrophic and Ekman flow components are utilized as pseudo-labels during Stages 1 and 2. Subsequently, Stage 3 relies entirely on physical constraints to execute the separation of the ageostrophic components. Detailed parameter configurations for the proposed AC-PIDNN model are provided in Supplementary Table S1.

3.3 Ageostrophic Current Component Decomposition

The ocean current field V_{total} predicted by PINN contains the component of geostrophy ($\vec{V}_{geo}$), wind stress ($\vec{V}_{ekman}$), and nonlinearity ($\vec{V}_{adv}$):

$$\vec{V}_{total} = \vec{V}_{geo} + \vec{V}_{adv} + \vec{V}_{ekman} \tag{15}$$

Where $\vec{V}_{total}$ is the velocity vector predicted by AC-PIDNN, $\vec{V}_{geo}$ is the geostrophic current from AVISO data and $\vec{V}_{ekman}$ is surface Ekman current in GLOBCURRENT data. Thus, the ADV, COR and WIND effect in Equation (1-2) is represented as $f\vec{k} \times \vec{V}_{adv}$, $f\vec{k} \times \vec{V}_{total}$, and $f\vec{k} \times \vec{V}_{ekman}$. To verify the balance of the predicted u_{total} and v_{total} from AC-PIDNN, the following balance was examined:

$$Bal_x = COR_x + PGF_x + WIND_x + ADV_x \tag{16}$$

$$Bal_y = COR_y + PGF_y + WIND_y + ADV_y \tag{17}$$

$$Bal = \left(\left(\frac{Bal_x}{PGF_x}\right)^2 + \left(\frac{Bal_y}{PGF_y}\right)^2\right)^{\frac{1}{2}} \tag{18}$$

Which quantifies the normalized residual of the balance in Equation (1-2). It is worth noting that, the Bal in this study is not intended as an independent external validation metric, but rather as a core self-consistency standard ensuring internal physical consistency. The minimization of this residual strictly validates that the extracted non-linear advection terms satisfy the physical equation constraints.

4 Results and Discussions

4.1 Validation of reconstructed currents and dynamical consistency

4.1.1 Dynamical consistency

This study employed the AC-PIDNN to reconstruct the daily global sea surface circulation from 1993 to 2023, incorporating geostrophic, nonlinear advective and Ekman-corrected components. The 30-year mean dynamical consistency of the AC-PIDNN-reconstructed surface circulation was evaluated by examining the zonal (Bal_x) and meridional (Bal_y) balances, together with the ratio of the residual magnitude to the pressure gradient force (Bal) (Fig.2 (a-c)). The residuals are generally small over most of the global ocean, with typical magnitudes on the order of 10^{-6} m s^{-2}. Relatively larger residuals are mainly confined to regions characterized by strong currents and energetic mesoscale variability, including western boundary current extensions and parts of the Southern Ocean. Despite these localized enhancements, the overall balance index Bal remains below 5%, indicating that the reconstructed surface circulation satisfies the surface momentum balance to a high degree across the global ocean. The Fig.2 (d) illustrates the temporal evolution of the globally averaged Bal from 1993 to 2023. The global mean value remains stable over the entire period, with the global mean $\pm$standard deviation range varies between 1%~1.5%. No systematic drift or long-term trend is evident, demonstrating that the correction maintains a consistent level of dynamical balance throughout the multi-decadal record. Figures S1 and S2 in the Supplementary Material show the momentum balance (Bal) evolution from Stage 1 to Stage 3 of the AC-PIDNN model's training, as well as comparisons with in-situ measurements and the Ocean Surface Current Analyses Real-time (OSCAR) dataset, validating the strong accuracy of the AC-PIDNN corrections. Together, these results confirm that the AC-PIDNN correction yields a surface circulation that is dynamically self-consistent and temporally robust.

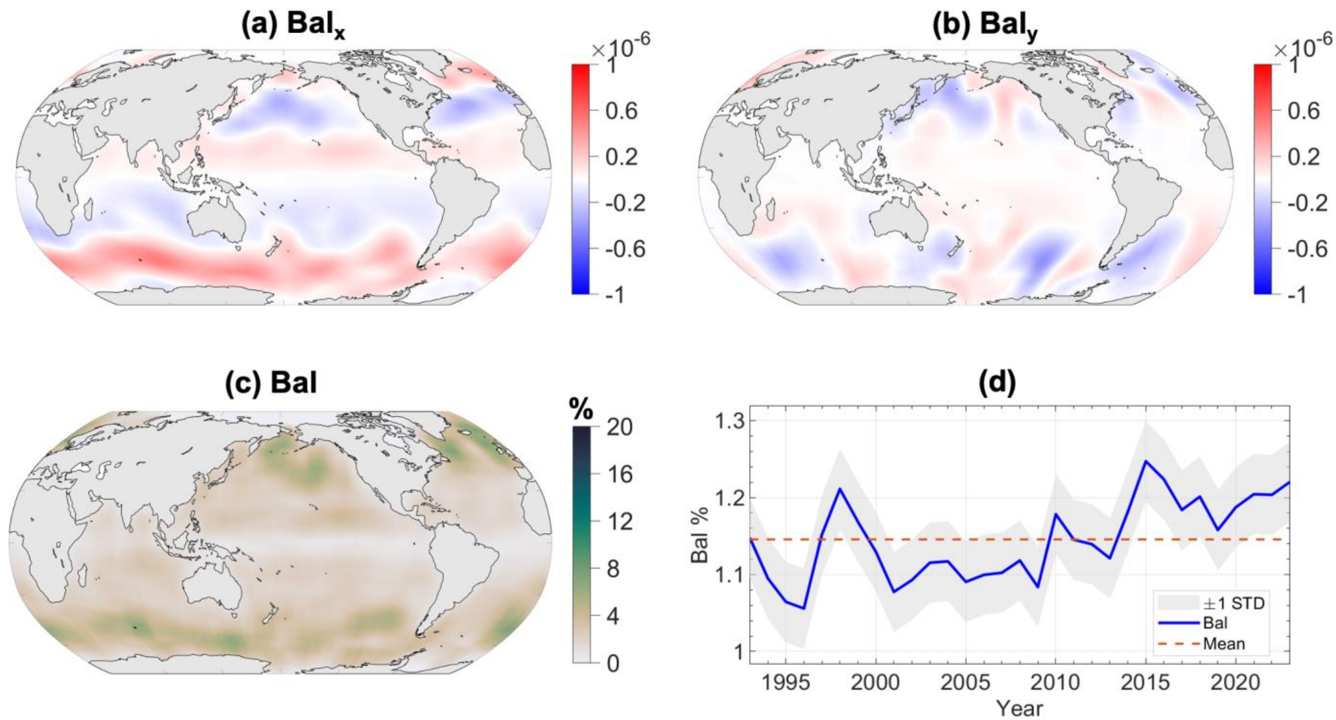

Figure 2: Balance analysis of the corrected 30-year means flow field within the momentum equations (4) and (5). Panel (a) 30-year mean residual of the zonal momentum equation, Bal_x (m s^{-2}), from 1993 to 2023; Panel (b) 30-year mean residual of the meridional momentum equation, Bal_y, from 1993 to 2023; Panel (c) 30-year mean ratio of the magnitude of the momentum equation residuals to the pressure gradient force, Bal, from 1993 to 2023. Panel (d) Time evolution of the globally averaged Bal from 1993 to 2023, with the shaded area representing the ±1 standard deviation range.

4.1.2 Comparison of AC-PIDNN Corrected Flow Fields and OSCAR Products Against In-Situ Data

To comprehensively validate the reliability and applicability of the AC-PIDNN dataset across different dynamical regimes globally, a systematic evaluation was conducted using widespread in-situ observations, alongside a multi-region comparative analysis with the existing OSCAR surface current product (1993-2022) downloaded from https://www.esr.org/data-products/oscar/. The in-situ data used for validation are derived from the tropical mooring buoy arrays, comprising the TAO array in the Pacific Ocean, the PIRATA array in the Atlantic Ocean, and the RAMA array in the Indian Ocean. As shown in Figure 3(a), a total of 54 observation stations widely distributed across the Pacific Ocean (21 stations), Atlantic Ocean (14 stations), and Indian Oceans (19 stations) (downloaded from https://www.pmel.noaa.gov/tao/drupal/disdel/).

The Root Mean Square Error (RMSE) was utilized to evaluate the AC-PIDNN-corrected total currents, OSCAR currents, geostrophic currents (Geo), and Ekman-corrected currents (Figure 3(b)–(d)). Statistical results demonstrate that across all three major ocean basins, the surface circulations corrected by AC-PIDNN are significantly closer to the in-situ observations compared to the traditional geostrophic and Ekman-corrected components. Specifically, in the Pacific Ocean, the RMSE of the AC-PIDNN-corrected current is 0.16 m/s, which outperforms the Ekman-corrected (0.24 m/s), geostrophic (0.22 m/s), and standard OSCAR product (0.19 m/s) currents, achieving an error reduction of approximately 15.8% relative to OSCAR. In the Indian Ocean, the AC-PIDNN RMSE is 0.10 m/s, outperforming both the Ekman-corrected (0.13 m/s) and geostrophic (0.15 m/s) currents, with a 23.1% error reduction compared to OSCAR (0.13 m/s). In the Atlantic Ocean, the AC-PIDNN RMSE is 0.15 m/s, which is lower than the Ekman-corrected (0.22 m/s) and geostrophic (0.17 m/s) currents, representing an 11.8% error reduction compared to OSCAR (0.17 m/s). Furthermore, the supplementary material provides time-series comparisons of the in-situ measured currents against the AC-PIDNN-corrected flow fields, OSCAR products, as well as the geostrophic and Ekman-corrected components at 28 stations. In summary, the basin-wide validation using these 54 independent stations conclusively demonstrates that the AC-PIDNN dataset delivers consistent and robust accuracy across all three major global oceans.

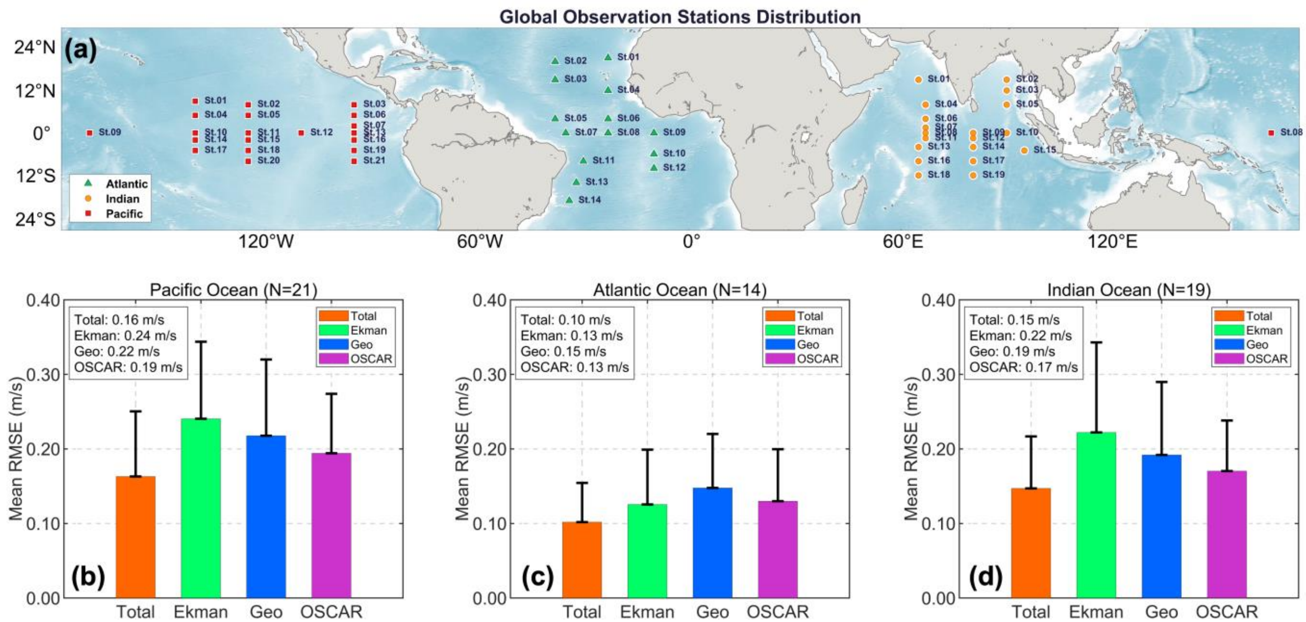

Figure 3: (a) Spatial distribution of TAO/PIRATA/RAMA mooring sites across the Pacific, Atlantic, and Indian Oceans. In-situ observation stations in each ocean basin are individually numbered to facilitate subsequent comparative experiments. (b)–(c) Bar charts illustrating the averaged root-mean-square error (RMSE) between TAO/PIRATA/RAMA mooring observations, OSCAR products and the AC-PIDNN-corrected current fields, geostrophic currents, and Ekman-corrected currents for the Pacific, Atlantic, and Indian Oceans, respectively.

To further evaluate the spatial distribution characteristics of the errors, a latitudinal error analysis of the AC-PIDNN and OSCAR surface current products was conducted using the in-situ observations. As illustrated in Fig.4, within the latitudinal range of approximately ±25° (corresponding to the spatial coverage of the deployed observation arrays), the AC-PIDNN-corrected dataset consistently outperforms the OSCAR product in matching the in-situ measurements. The analysis reveals that larger errors are predominantly concentrated in the equatorial band (within a latitude range of approximately ±5°). Conversely, accuracy improves significantly in mid-to-low latitudes and regions further from the equator, aligning much more closely with field observations. Specifically, the RMSE decreases gradually from 0.25 m/s near the equator to 0.05 m/s in the higher-latitude observation areas. Overall, within the ±25° latitudinal band, the AC-PIDNN product consistently demonstrates better performance than the OSCAR product, indicating that the improved reliability of the dataset is not an isolated artifact but a geographically consistent feature across a broad spatial extent. Additionally, it should be noted that due to the limited spatial coverage of current continuous in-situ observation arrays, there is presently a lack of robust comparison in high-latitude regions.

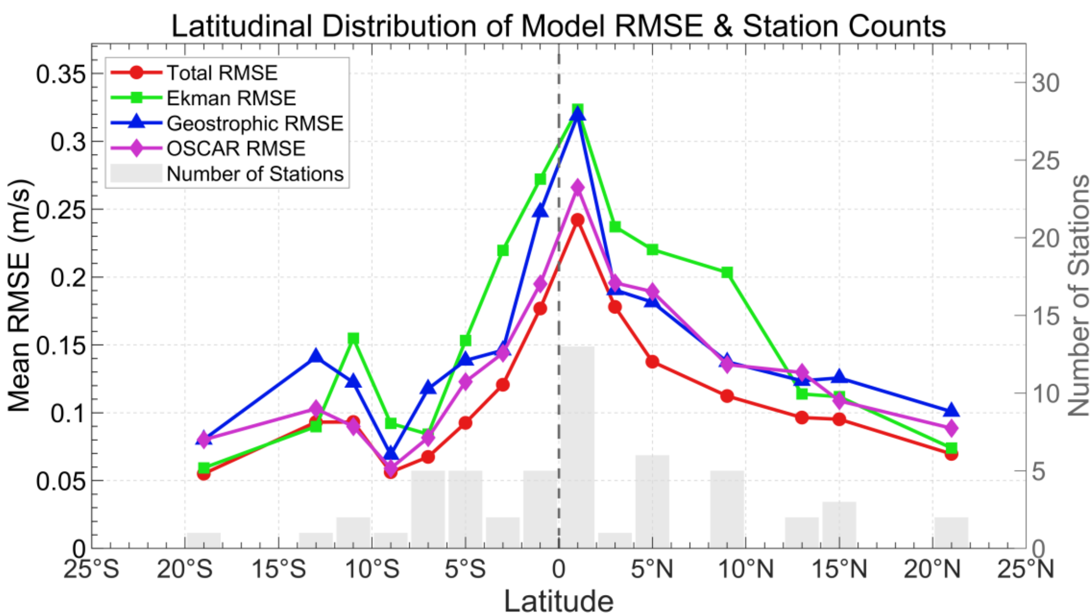

Figure 4: presents the latitudinal error curves of the in-situ measurements against both the corresponding AC-PIDNN-corrected currents and the OSCAR products across the 54 observation stations.

4.1.3 Comparison of AC-PIDNN Corrected Flow Fields Against ROMS data

To further evaluate the reconstruction accuracy, we conducted an additional validation using a high-resolution ROMS simulation as an independent reference. In this experiment, the ROMS-simulated sea surface height was used as the sole input to reconstruct the surface velocity field, ensuring a fair comparison between the baseline iterative method and the AC-PIDNN approach. As the ROMS simulation used herein neglects the Ekman component, this component is not taken into account in the present study. Figure 5 compares the reconstructed surface velocity fields with the ROMS reference in the northwestern Pacific Ocean. The zonal (u) and meridional (v) velocity components, as well as the velocity magnitude, are shown for the ROMS simulation, the Iteration method, and the AC-PIDNN reconstruction. The Iteration method reproduces the general structure of the velocity fields but exhibits substantial amplitude mismatches, particularly in regions of strong currents and mesoscale activity, with RMSE values of 0.12 m s^{-1} for u and 0.16 m s^{-1} for v, and 0.11 m s^{-1} for the magnitude of the velocity over the mapped domain. In contrast, the AC-PIDNN reconstruction reproduces the dominant spatial structures of the surface circulation more faithfully. The pathway and intensity of the western boundary current, as well as the surrounding mesoscale features, are captured with improved spatial coherence. Correspondingly, the RMSE is reduced to approximately 0.01 m s^{-1} for both velocity components and for the velocity magnitude, representing nearly an order-of-magnitude improvement over the iterative approach. Together with the momentum-balance diagnostics, the ROMS-based validation confirms that the corrected surface circulation is both dynamically consistent and quantitatively accurate under controlled conditions.

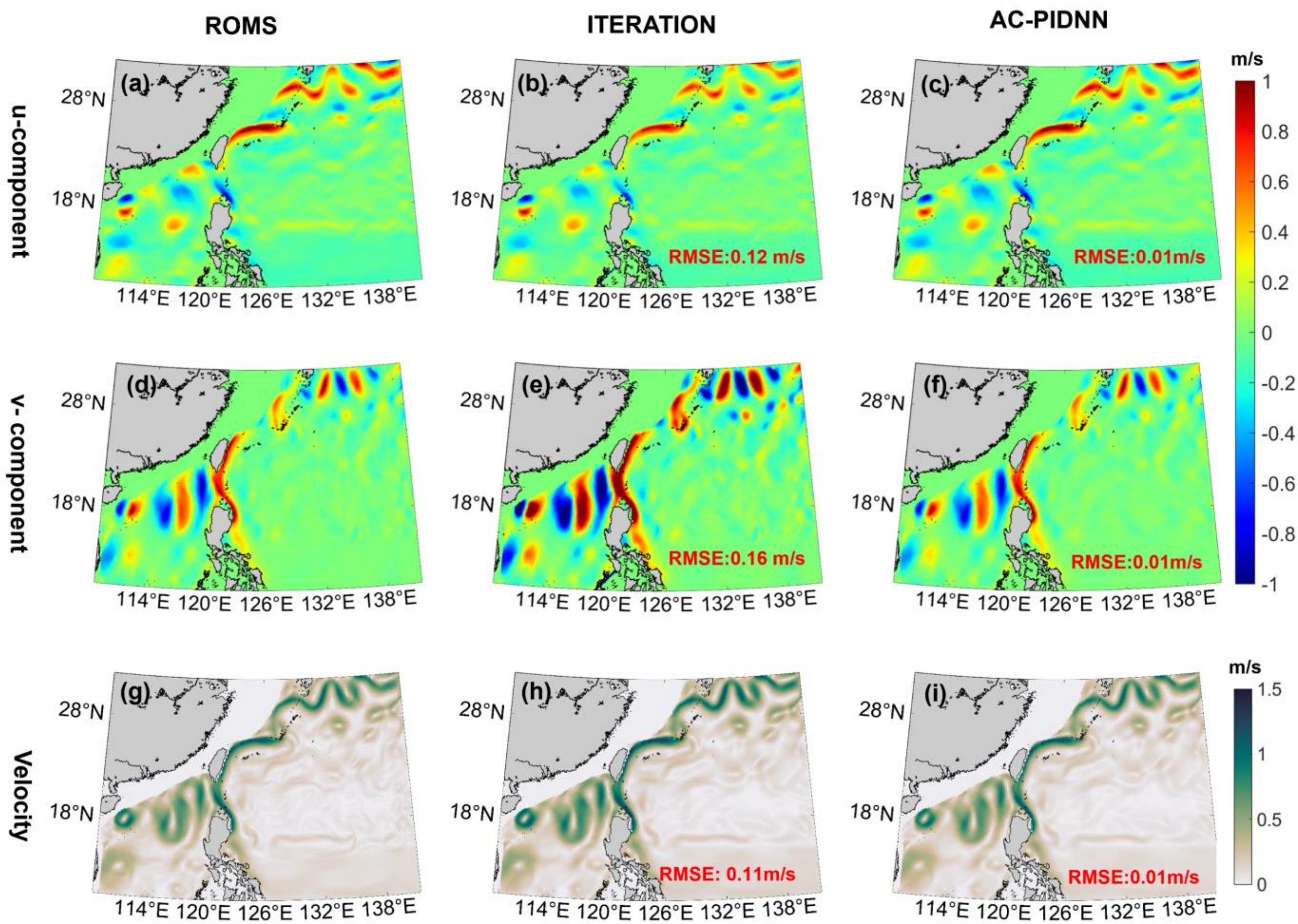

Figure 5: Sea Surface Flow Field after Correction of Sea Surface Height Anomalies in the Northwestern Pacific using Iterative Method and AC-PIDNN. The first column shows the u-component, v-component, and flow field of the simulated data; the second column show the results corrected by the iterative method and AC-PIDNN method.

4.2 Characteristics of the corrected surface circulation

In this section, we decompose the daily surface circulation (1993–2023) into geostrophic ($\vec{V}_{geo}$), Ekman-corrected ($\vec{V}_{Ekman}$), nonlinear advective ($\vec{V}_{adv}$) components. The detailed results for the Kuroshio region and the equatorial Pacific region are shown in Fig.S4 and S5, respectively. For each component, we analysed the zonal and meridional velocity components (u and v) together with the flow speed (Fig. 6).

The nonlinear advective component (Fig.6 (a–c)) exhibits a relatively smaller magnitude. Both its zonal and meridional contributions are generally on the order of 10^{-2} m s^{-1}, with elevated values confined to dynamically active regions. These localized enhancements are most evident along the equatorial band, within western boundary current systems and their extensions, and over parts of the Southern Ocean (Qiu et al., 2014). Over the majority of the open ocean, the advective component remains weak, indicating that its contribution to the corrected surface circulation is primarily expressed through regional and localized modulation rather than basin-scale influence. The Ekman-corrected component (Fig.6 (d–f)) displays a clear large-scale organization. Its zonal and meridional velocities show pronounced latitudinal banding over wide areas of the tropics and subtropics, consistent with the distribution of large-scale wind forcing. Typical Ekman-corrected velocities reach $\boldsymbol{O}(10^{-1})$ m s^{-1} in low- and mid-latitude regions, with reduced magnitudes toward higher latitudes.

The large-scale structure and intensity of the surface circulation are primarily controlled by the geostrophic flow (Fig.6 (g–i)). Both zonal and meridional geostrophic velocities exhibit strong signals associated with major current systems, including western boundary currents and their extensions and the Antarctic Circumpolar Current. The geostrophic speed commonly reaches $\boldsymbol{O}(10^{-1}$ -$10^{0})$ m s^{-1}. The weaker values are found in the interiors of subtropical gyres. As a result of the combined contributions, the total surface velocity field (Fig.6 (j–l)) closely resembles the geostrophic circulation in its overall structure, while exhibiting systematic modifications in both magnitude and spatial details. In particular, westward zonal flow near the equator and Southern Ocean, and meridional transport in adjacent regions are strengthened relative to a purely geostrophic approximation, highlighting the cumulative influence of Ekman-corrected and nonlinear advective processes in shaping the corrected surface circulation. Neglecting these ageostrophic components would therefore bias the spatial distribution and magnitude of reconstructed surface currents.

Because the total velocity is defined as the linear sum of the three components, this decomposition provides a natural basis for examining their respective contributions to commonly used kinematic and energetic diagnostics, as discussed in the following section.

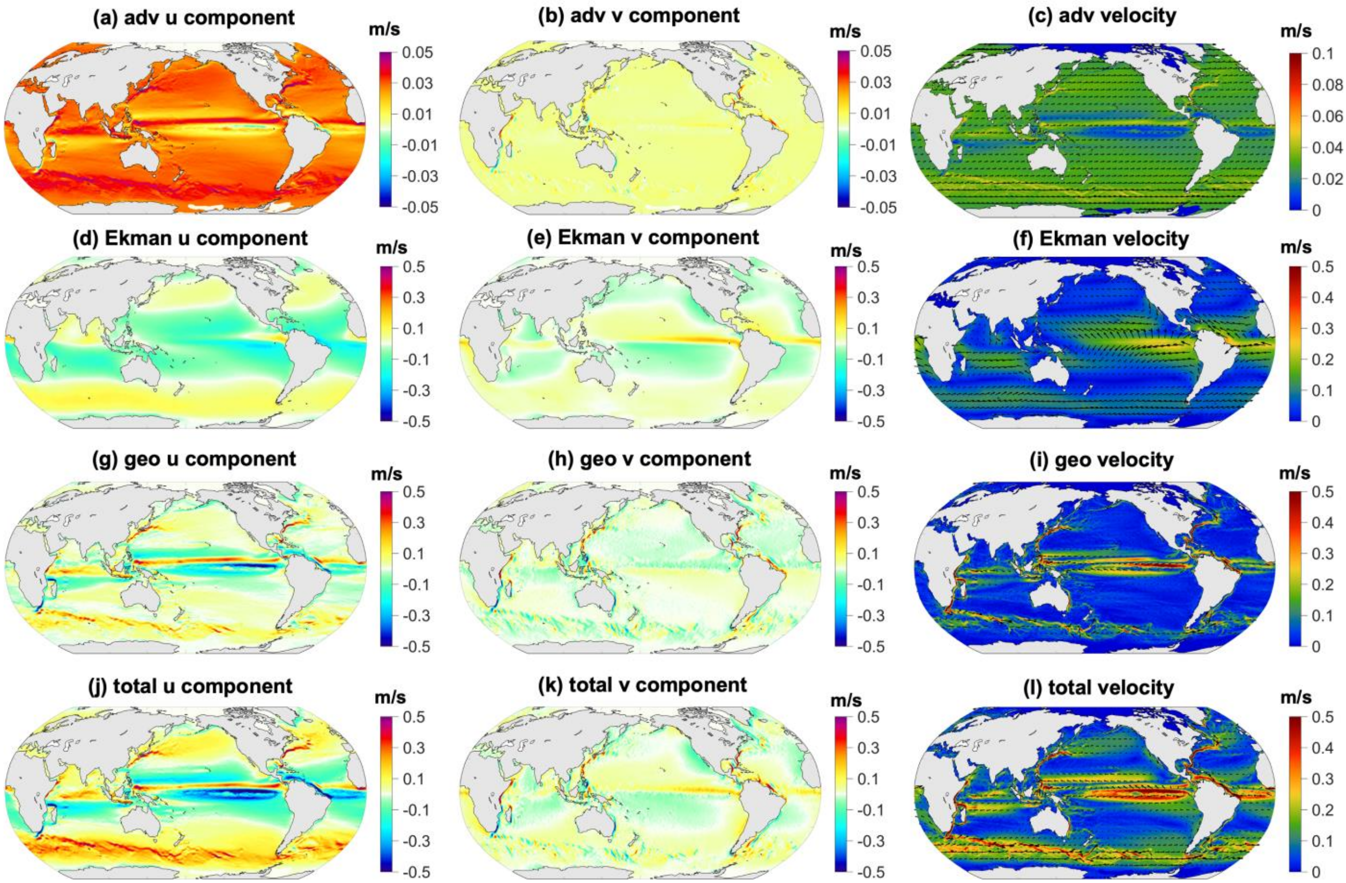

Figure 6: Results of Sea Surface Circulation Correction from 1993 to 2023, using the AC-PIDNN model, incorporating geostrophic, nonlinear advective and Ekman-corrected components. Panels (a)–(c) show the u-component, v-component, and flow field of the nonlinear advective component; Panels (d)–(f) show the u-component, v-component, and flow field of the Ekman-corrected component; Panels (g)–(i) show the u-component, v-component, and flow field of the geostrophic component; Panels (J)–(L) show the u-component, v-component, and flow field of the total circulation.

4.3 Impacts on kinematic and energetic diagnostics

This section examines the impacts of the velocity correction on commonly used kinematic and energetic diagnostics, including surface relative vorticity (VOR), divergence (DIV), and eddy kinetic energy (EKE). These variables are widely applied in studies of upper-ocean dynamics (Wunsch, 2025) and therefore provide an important perspective on the implications of the corrected surface circulation.

$$VOR = \frac{\partial v}{\partial x} - \frac{\partial u}{\partial y} \tag{19}$$

$$DIV = \frac{\partial u}{\partial x} + \frac{\partial v}{\partial y} \tag{20}$$

$$EKE = \frac{1}{2}\left(u'^2 + v'^2\right) \tag{21}$$

4.3.1 Vorticity

Sea surface relative vorticity is a key dynamical parameter that describes the rotational characteristics of the upper ocean flow, directly linked to flow shear, vortex structures, and angular momentum distribution (Zhang et al., 2024; Kwak and Richmond, 2014). The geostrophic component (Fig.7 (c)) dominates the large-scale structure of the relative vorticity field. Regions of strong positive and negative vorticity are closely aligned with major current systems, including western boundary currents, their downstream extensions, and the Antarctic Circumpolar Current. This distribution outlines the primary rotational framework of the surface circulation and reflects the strong shear associated with geostrophic jets and frontal zones. In addition to the geostrophic component, the wind-driven Ekman flow contributes significantly to the sea surface relative vorticity. Here, the Ekman-corrected component refers specifically to the vorticity generated by the velocity field that balances the wind stress forcing in the horizontal momentum equations (i.e., the Ekman flow), as distinct from the vertical Ekman pumping velocity associated with wind stress curl (Chen et al., 2020). While generally weaker in magnitude than geostrophic vorticity, this component exhibits distinct regional signatures. Enhanced Ekman vorticity (Fig.7 (b)) is particularly evident in tropical and subtropical basins where winds are strong and relatively steady, such as the trade wind belts and prevailing westerlies, where lateral shear in the Ekman-corrected velocity can generate significant vorticity signals (Chen et al., 2020). For instance, in equatorial regions, zonal wind stress can excite pronounced Ekman vorticity anomalies due to the variation of the Coriolis parameter. In contrast, the nonlinear vorticity (Fig.7 (a)) term arising from advection by the flow itself is typically about two orders of magnitude smaller in strength than the geostrophic and -corrected components. However, in regions of intense currents and strong shear, such as the Kuroshio Extension and Gulf Stream separation zones, nonlinear processes become crucial in modulating vorticity variability, energy cascade, and submesoscale vortex activities, and thus cannot be neglected(Chen et al., 2020). We present the 30-year average vorticity for the western boundary Kuroshio region and the wind-forced equatorial Pacific current region in Supplementary Fig.S6 (a-d) and Fig.S7 (a-d), respectively. This indicates that while the foundational structure of the large-scale vorticity field is set by geostrophic balance, with wind forcing and nonlinear dynamics providing an additional contribution to vorticity magnitude particularly in dynamically active regions.

4.3.2 Divergence

Sea surface horizontal divergence is a key physical quantity characterizing the divergent/convergent nature of the upper-ocean flow, with important implications for mass transport (Dubois et al., 2016). Unlike the vorticity field, the dynamical components of the divergence field exhibit distinct and contrasting contributions. From a dynamical decomposition perspective, the horizontal divergence of the geostrophic component (Fig.7 (g)) is negligible at the sea surface under the continuum layer approximation, dictated by its non-divergent nature. Thus, the geostrophic flow contributes insignificantly to the large-scale sea surface horizontal divergence. In contrast, the nonlinear advective component (Fig.7 (e)) dominates the large-scale spatial pattern of the divergence field. Its magnitude is substantially larger than other components, forming prominent bands of divergence/convergence in regions of strong currents (e.g., western boundary current extensions) and vigorous eddy activity. It is noteworthy that although the local amplitude of the advective divergence is large, its net contribution to basin-scale or global integrated divergence is modest due to the cancellation between extensive positive and negative regions. The Ekman-corrected component of divergence (Fig.7 (f)), however, originates directly from Ekman pumping/suction driven by wind stress curl. Its local intensity is typically weaker than the advective component. Due to its more spatially coherent sign (e.g., divergence over regions of positive wind stress curl and convergence over negative curl regions), the Ekman-corrected component contributes significantly to the domain-averaged or net divergent effect at regional or global scales, and its magnitude is non-negligible. For instance, in the major wind belts (trade winds, westerlies), Ekman divergence forms a key driver for large-scale vertical circulation cells, such as the subtropical gyres (Roquet et al., 2025). To further illustrate the impacts of nonlinear processes and wind forcing on sea surface divergence, we present the 30-year average vorticity for the western boundary Kuroshio region and the wind-forced equatorial Pacific current region in Supplementary Fig.S6 (e-h) and Fig.S7 (e-h), respectively.

4.3.3 Eddy Kinetic Energy

Eddy Kinetic Energy is an integrated metric for the intensity of mesoscale variability, representing the perturbation energy of the flow velocity field relative to its temporal mean. It serves as a key parameter for assessing the energetic consistency and dynamical plausibility of the corrected velocity field (Huo et al., 2024). As shown in Fig.7 (i-l) the global EKE distribution derived from the corrected circulation field, which incorporates geostrophic, Ekman-corrected, and nonlinear advective components exhibits the well-documented pattern of high-energy regimes: primarily concentrated in western boundary current extensions (e.g., the Kuroshio Extension, Gulf Stream Extension), the core regions of the Antarctic Circumpolar Current, and equatorial current systems, all areas of high dynamical activity (Su et al., 2023). To further illustrate this point, Supplementary Fig.S6 (i-l) and Fig.S7 (i-l) present the 30-year mean EKE characteristics in the equatorial Pacific region and the Kuroshio region, respectively. These energetic hotspots are closely linked to strong shear, instability processes, and active mesoscale eddy generation. Compared to EKE estimates based solely on the geostrophic approximation, the inclusion of the Ekman and nonlinear advective components does not introduce spurious amplification of the total kinetic energy. Instead, it redistributes the energy spatially in a physically consistent manner. The correction primarily modulates the structure of the EKE field rather than significantly altering its global intensity magnitude. Specifically, in regions where wind forcing is pronounced, such as the equatorial and subtropical zones, incorporating the Ekman-corrected component provides a more realistic representation of fluctuating energy directly generated by wind variability. Meanwhile, in the vicinity of strong current edges and frontal zones, nonlinear advective processes dominate in shaping the fine-scale structure of EKE, such as energy cascade and eddy-mean flow interactions (Adeagbo et al., 2022). In summary, the multi-component velocity correction scheme redistributes the spatial pattern of EKE in a manner consistent with physical mechanisms while preserving the overall energetic framework of the surface circulation. This enhances the capability of the EKE field to characterize mesoscale processes, energy transfer pathways, and mixing efficiency, yielding a representation that is closer to the true dynamical context of the ocean.

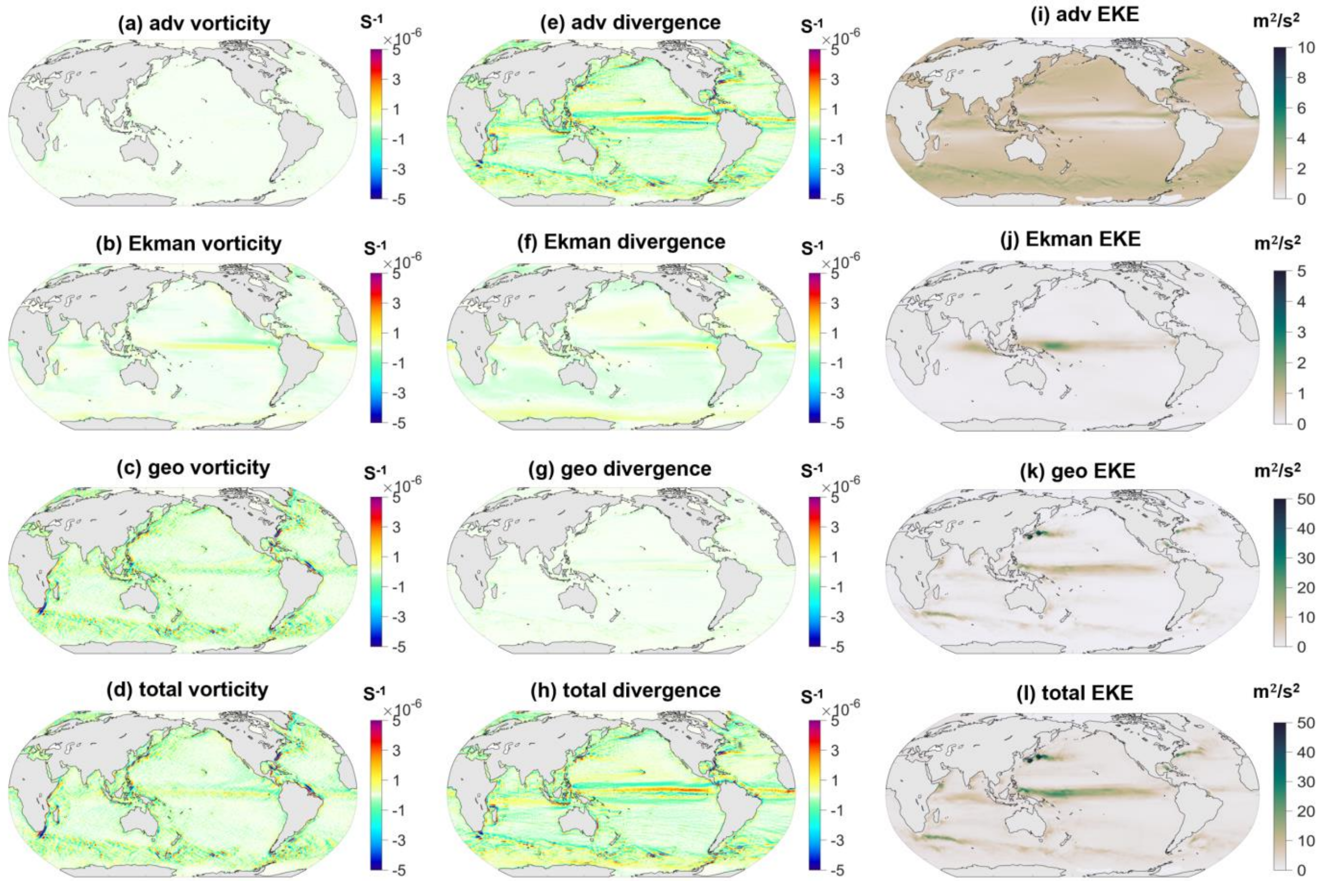

Figure 7: 30-year average global sea surface dynamic parameter characteristics. Panels (a)–(d) showing the vorticity of the advective, Ekman-corrected, geostrophic, and total components, respectively; Panels (e)–(h) showing the divergence of the advective, Ekman-corrected, geostrophic, and total components, respectively; Panels (i)–(l) showing the eddy kinetic energy (EKE) of the advective, Ekman-corrected, geostrophic, and total components, respectively.

4.3.4 Temporal Evolution of Dynamical Diagnostics

To analyze the long-term variations in the three dynamic parameters mentioned above, Fig.8 presents the 30-year averaged time series for the global ocean, the Kuroshio region (110°E–175°E, 12°N–50°N), and the Equatorial Current region (60°W–110°E, 20°S–20°N). On a global scale (Fig.8 (a-c)), the interannual variability of total divergence ($\boldsymbol{O}(10^{-8})$ s^{-1}) is primarily dominated by the Ekman-corrected component ($\boldsymbol{O}(10^{-9})$ s^{-1}), with the nonlinear component ($\boldsymbol{O}(10^{-9})$ s^{-1}) also contributing significantly, and their variation trends are largely consistent. The magnitude of variability in nonlinear divergence is smaller than that of the Ekman-corrected component but significantly larger than the negligible geostrophic divergence ($\boldsymbol{O}(10^{-10})$ s^{-1}). The total relative vorticity field ($\boldsymbol{O}(10^{-9})$ s^{-1}) is mainly determined by the combined effects of the geostrophic component ($\boldsymbol{O}(10^{-9})$ s^{-1}) and the Ekman-corrected component ($\boldsymbol{O}(10^{-10})$ s^{-1}). In terms of trends, the Ekman-corrected vorticity exhibits a weakening trend, whereas both geostrophic and total vorticities show a long-term enhancement of negative vorticity. No significant interannual signal is detected in nonlinear vorticity. Regarding eddy kinetic energy (EKE), the trend in total EKE aligns with that of geostrophic EKE but is notably modulated by nonlinear processes. Moreover, the magnitudes of the nonlinear and geostrophic components are comparable, with the nonlinear EKE being higher in most years, yet both remain within the same order of magnitude ($\boldsymbol{O}(10^{0}–10^{1})$ m^2 s^{-2}).

On a regional scale, two representative areas, the Kuroshio region and the Equatorial Current region are selected for analysis (Fig.8 (d-i)). In the Kuroshio region, the variation in total divergence follows the trend of the nonlinear component, although the contribution of the Ekman-corrected component is non-negligible, particularly in equatorial areas. The magnitude of divergence in the Kuroshio region ($\boldsymbol{O}(10^{-8})$ s^{-1}) is larger than that in the Equatorial Current region ($\boldsymbol{O}(10^{-9})$ s^{-1}). Regarding vorticity, the Kuroshio region is dominated by negative vorticity, with the absolute value of the Ekman-corrected component being significantly larger than that of the geostrophic component. In contrast, the Equatorial Current region exhibits positive Ekman-corrected vorticity and negative geostrophic vorticity, with total vorticity primarily contributed by the Ekman-corrected component. Additionally, the magnitudes of geostrophic and total vorticities in the Kuroshio region ($\boldsymbol{O}(10^{-8})$ s^{-1}) exceed those in the Equatorial Current region ($\boldsymbol{O}(10^{-9})$ s^{-1}). For EKE, variations in both regions are mainly governed by the geostrophic component. The trend in total EKE in the Equatorial Current region closely resembles that of its geostrophic component, whereas the Kuroshio region has shown an increasing trend in EKE since approximately 2017. In terms of magnitude, total EKE, geostrophic EKE, and nonlinear EKE are all on the order of $\boldsymbol{O}(10^{0}–10^{1})$ m^2 s^{-2}. The Ekman-corrected EKE in the Equatorial Current region ($\boldsymbol{O}(10^{-1})$ m^2 s^{-2}) is larger than that in the Kuroshio region ($\boldsymbol{O}(10^{-2})$ m^2 s^{-2}).

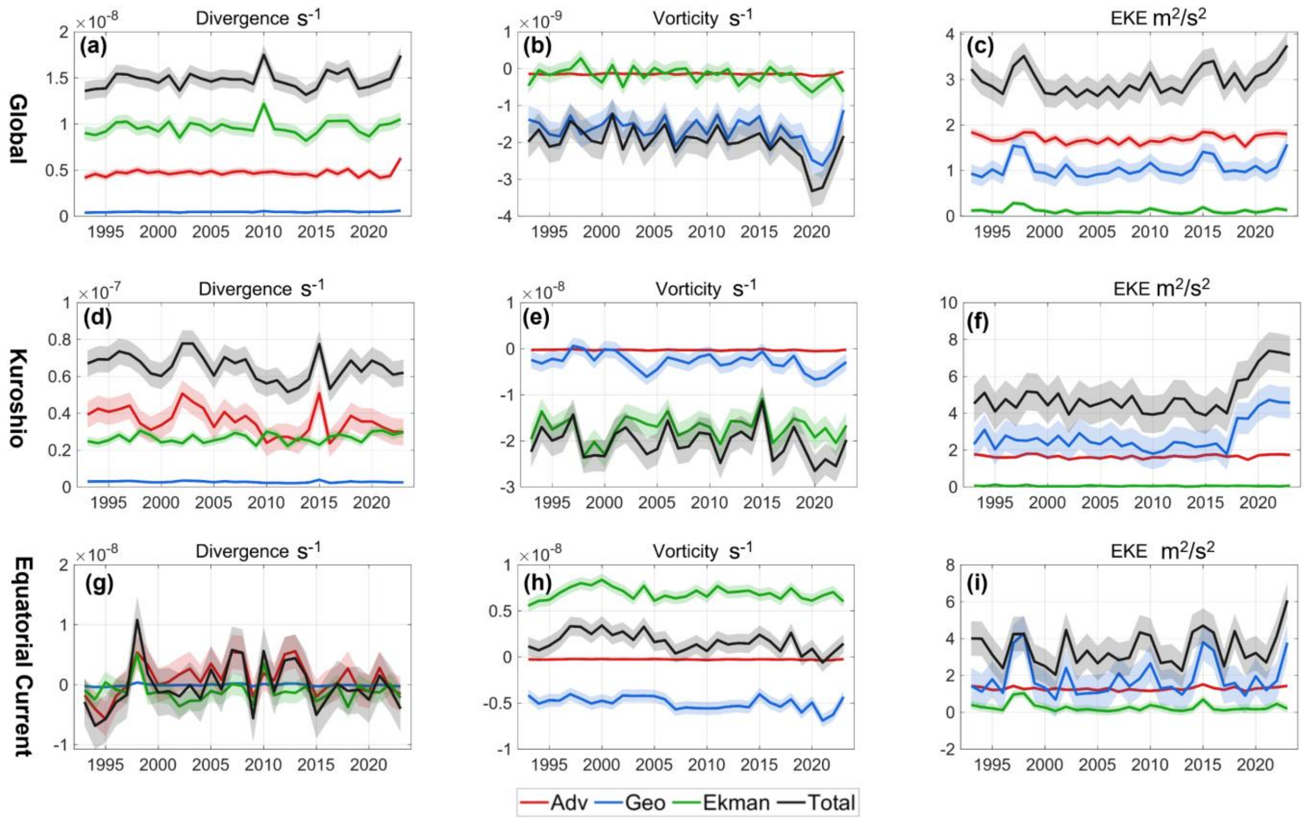

Figure 8: The annual mean variations in sea surface divergence, vorticity, and EKE from 1993 to 2023 for the global ocean, the Kuroshio region, and the equatorial current region. Panels (a)–(c) illustrate the interannual changes in globally averaged sea surface divergence, vorticity, and EKE; Panels (d)–(f) show the corresponding variations in the Kuroshio region (110°–175°E, 12°–50°N); and panels (g)–(l) display the changes in the equatorial current region (60°W–110°E, 20°S–20°N). The shaded area around each curve represents the ±1 standard deviation range.

5 Code and data availability

The code for AC-PIDNN is available at **https://github.com/cgxcgxcgxcgx/AC-PIDNN.** The global sea surface circulation dataset corrected for the period 1993–2023 in this study can be accessed via **https://zenodo.org/records/19966716** (Cui and Cai, 2026). This dataset has a spatial resolution of 0.25°, and each daily flow field file contains the variable names and their descriptions as listed in Table 1. Furthermore, the table outlines the Dataset ID corresponding to the satellite data product (global gridded geostrophic currents and surface Ekman currents) obtained from the Copernicus Marine Service at: https://data.marine.copernicus.eu/product.

Table 1 Dataset Variable Information

Values	size	definition	Dataset ID
sla	720×1440	Sea Level Anomaly, sourced from the AVISO dataset.	cmems_obs-sl_glo_phy-ssh_my_allsat-l4-duacs-0.125deg_P1D
ugeo	720×1440	Zonal (u) component of the geostrophic current, sourced from the AVISO dataset.	
vgeo	720×1440	Meridional (v) component of the geostrophic current, sourced from the AVISO dataset.	
uekman	720×1440	Zonal (u) component of the surface (0 m) Ekman current, sourced from the global Copernicus Ocean (GLOBCURRENT) surface and 15-meter Ekman and geostrophic current datasets.	cmems_obs-mob_glo_phy-cur_my_0.25deg_P1D-m
vekman	720×1440	Meridional (v) component of the surface (0 m) Ekman current, sourced from the global Copernicus Ocean (GLOBCURRENT) surface and 15-meter Ekman and geostrophic current datasets.	
uadv	720×1440	Zonal (u) component of the nonlinear advective term.	-
vadv	720×1440	Meridional (v) component of the nonlinear advective term.	-
utotal	720×1440	Zonal (u) component of the total flow field corrected by the AC-PIDNN model.	-
vtotal	720×1440	Meridional (v) component of the total flow field corrected by the AC-PIDNN model.	-
resu Resu	720×1440	Residual of the zonal (u) momentum (Navier-Stokes) equation.	-
resv Resv	720×1440	Residual of the meridional (v) momentum (Navier-Stokes) equation.	-
lon	1×1440	Longitude coordinates, ranging from -179.75°E to 180°E with a 0.25° resolution.	-
lat	720×1	Latitude coordinates, ranging from -89.75°N to 90°N with a 0.25° resolution.	-

6 Conclusions

A key contribution of this study is the development of a physics-informed deep learning framework to correct sea surface currents and quantify their dynamical components. By explicitly incorporating physical constraints, the framework substantially improves the dynamical consistency of reconstructed surface circulation and yields a global daily dataset for 1993-2023. Our results show that, although ageostrophic components are generally smaller than the geostrophic flow, they make important contributions to the total surface circulation, especially in energetic regions such as western boundary currents and the Kuroshio Extension. On a global scale, the mean velocity of the total flow field is on the order of $O(10^{-2}–10^{-1})$ m s^{-1}, with the Ekman-corrected, geostrophic, and nonlinear components each exhibiting magnitudes of $O(10^{-2})$ m s^{-1}. In particular, nonlinear contributions have limited influence on relative vorticity, as the dominant rotational structure is captured by the geostrophic circulation. In contrast, the nonlinear corrections strongly affect surface divergence and eddy kinetic energy, revealing aspects of ocean surface dynamics that are not captured by geostrophic circulation alone. These findings show that resolving ageostrophic dynamics is essential for a more complete understanding of global surface circulation and its variability.

Acknowledgement

This work was funded by the National Natural Science Foundation of China (42376024, 42450181), Science and Technology Development Fund, Macau SAR (File/Project no. 0093/2020/A2, 001/2024/SKL); This work is supported by Centre for Regional Oceans in University of Macau (SP2025-00005-CRO); This work is supported by CORE, which is a joint research center for ocean research between Laoshan Laboratory and HKUST, and substantially supported by a grant from the Research Grants Council of the Hong Kong Special Administrative Region, China (Project Reference Number: AoE/P-601/23-N). The simulation was performed at the SICC, which is supported by the SKL-IOTSC, University of Macau.

References

Adeagbo, O. S., Du, Y., Wang, T., and Wang, M.: Eddy–mean flow interactions in the Agulhas leakage region, Journal of Oceanography, 78, 151–161, 10.1007/s10872-022-00637-6, 2022.

Aluie, H., Hecht, M., and Vallis, G. K.: Mapping the Energy Cascade in the North Atlantic Ocean: The Coarse-Graining Approach, Journal of Physical Oceanography, 48, 225–244, https://doi.org/10.1175/JPO-D-17-0100.1, 2018.

Andres, M., Park, J.-H., Wimbush, M., Zhu, X.-H., Chang, K.-I., and Ichikawa, H.: Study of the Kuroshio/Ryukyu Current system based on satellite-altimeter and in situ measurements, Journal of Oceanography, 64, 937–950, https://doi.org/10.1007/s10872-008-0077-2, 2008.

Armitage, T. W. K., Bacon, S., Ridout, A. L., Petty, A. A., Wolbach, S., and Tsamados, M.: Arctic Ocean surface geostrophic circulation 2003–2014, The Cryosphere, 11, 1767–1780, https://doi.org/10.5194/tc-11-1767-2017, 2017.

Arnason, G., Haltiner, G., and Frawley, M.: Higher-order geostrophic wind approximations, Monthly Weather Review, 90, 175–185, https://doi.org/10.1175/1520-0493(1962)090<0175:HGWA>2.0.CO;2, 1962.

Bonino, G., Galimberti, G., Masina, S., McAdam, R., and Clementi, E.: Machine learning methods to predict sea surface temperature and marine heatwave occurrence: a case study of the Mediterranean Sea, Ocean Sci., 20, 417–432, https://doi.org/10.5194/os-20-417-2024, 2024.

Buckingham, C. E., Gula, J., and Carton, X.: The Role of Curvature in Modifying Frontal Instabilities. Part I: Review of Theory and Presentation of a Nondimensional Instability Criterion, Journal of Physical Oceanography, 51, 299–315, https://doi.org/10.1175/JPO-D-19-0265.1, 2021.

Cao, Y., Dong, C., Qiu, Z., Bethel, B. J., Shi, H., Lü, H., and Cheng, Y.: Corrections of Mesoscale Eddies and Kuroshio Extension Surface Velocities Derived from Satellite Altimeters, Remote Sensing, 15, https://doi.org/10.3390/rs15010184, 2023a.

Cao, Y., Dong, C., Stegner, A., Bethel, B. J., Li, C., Dong, J., Lü, H., and Yang, J.: Global Sea Surface Cyclogeostrophic Currents Derived From Satellite Altimetry Data, Journal of Geophysical Research: Oceans, 128, e2022JC019357, https://doi.org/10.1029/2022JC019357, 2023b.

Chen, K., Gaube, P., and Pallàs-Sanz, E.: On the Vertical Velocity and Nutrient Delivery in Warm Core Rings, Journal of Physical Oceanography, 50, 1557–1582, https://doi.org/10.1175/JPO-D-19-0239.1, 2020.

Cho, S. W., Choi, J. G., Kim, D., Lu, W., and Jo, Y. H.: Deriving hourly diagnostic surface velocity fields considering inertia and an application in the Yellow Sea, EGUsphere, 2025, 1–24, https://doi.org/10.5194/egusphere-2025-2748, 2025.

Cui, G. and Cai, Z.: Daily Global Sea Surface Ageostrophic Current Dataset from 1993–2023 via Physics-Informed Deep Learning [dataset], https://doi.org/10.5281/zenodo.19966716, 2026.

Cui, G., Cai, Z., and Liu, Z.: A hybrid physics-informed and data-driven model for estimating ocean internal wave phase speeds from remote sensing imagery, Remote Sensing of Environment, 335, 115247, https://doi.org/10.1016/j.rse.2026.115247, 2026.

Cui, G., Yuen, K.-V., Cai, Z., Liu, Z., and Zhang, G.: Research on adaptive ocean remote sensing target detection framework: An efficient solution based on the broad learning system, ISPRS Journal of Photogrammetry and Remote Sensing, 229, 188–210, https://doi.org/10.1016/j.isprsjprs.2025.08.020, 2025.

Dong, C., Xu, G., Han, G., Bethel, B. J., Xie, W., and Zhou, S.: Recent Developments in Artificial Intelligence in Oceanography, Ocean-Land-Atmosphere Research, 2022, https://doi.org/10.34133/2022/9870950, 2022.

Douglass, E. M. and Richman, J. G.: Analysis of ageostrophy in strong surface eddies in the Atlantic Ocean, Journal of Geophysical Research: Oceans, 120, 1490–1507, https://doi.org/10.1002/2014JC010350, 2015.

Du, Y., Dong, X., Jiang, X., Zhang, Y., Zhu, D., Sun, Q., Wang, Z., Niu, X., Chen, W., and Zhu, C.: Ocean surface current multiscale observation mission (OSCOM): Simultaneous measurement of ocean surface current, vector wind, and temperature, Progress in Oceanography, 193, 102531, https://doi.org/10.1016/j.pocean.2021.102531, 2021.

Dubois, M., Rossi, V., Ser-Giacomi, E., Arnaud-Haond, S., López, C., and Hernández-García, E.: Linking basin-scale connectivity, oceanography and population dynamics for the conservation and management of marine ecosystems, Global Ecology and Biogeography, 25, 503–515, https://doi.org/10.1111/geb.12431, 2016.

Edwards, C. A., De Mey-Frémaux, P., Barceló-Llull, B., Charria, G., Choi, B.-J., Halliwell, G. R., Hole, L. R., Kerry, C., Kourafalou, V. H., Kurapov, A. L., Moore, A. M., Mourre, B., Oddo, P., Pascual, A., Roughan, M., Skandrani, C., Storto, A., Vervatis, V., and Wilkin, J. L.: Assessing impacts of observations on ocean circulation models with examples from coastal, shelf, and marginal seas, Volume 11 - 2024, https://doi.org/10.3389/fmars.2024.1458036, 2024.

Fan, S., Kudryavtsev, V., Yurovsky, Y., and Zhang, B.: Reconstructing ocean surface current vector field from SAR doppler shift measurements, Remote Sensing of Environment, 328, 114855, https://doi.org/10.1016/j.rse.2025.114855, 2025.

Fraser, N. J., Fox, A. D., Cunningham, S. A., Rath, W., Schwarzkopf, F. U., and Biastoch, A.: Vertical Velocity Dynamics in the North Atlantic and Implications for AMOC, Journal of Physical Oceanography, 54, 2011–2024, https://doi.org/10.1175/JPO-D-23-0229.1, 2024.

Glorot, X. and Bengio, Y.: Understanding the difficulty of training deep feedforward neural networks, JMLR Workshop and Conference Proceedings, 9, 249–256, 2010.

Hiron, L., Nolan, D. S., and Shay, L. K.: Study of Ageostrophy during Strong, Nonlinear Eddy-Front Interaction in the Gulf of Mexico, Journal of Physical Oceanography, 51, 745–755, https://doi.org/10.1175/JPO-D-20-0182.1, 2021.

Huo, J., Zhang, J., Yang, J., Li, C., Liu, G., and Cui, W.: High kinetic energy mesoscale eddy identification based on multi-task learning and multi-source data, International Journal of Applied Earth Observation and Geoinformation, 128, 103714, https://doi.org/10.1016/j.jag.2024.103714, 2024.

Ioannou, A., Stegner, A., Tuel, A., LeVu, B., Dumas, F., and Speich, S.: Cyclostrophic Corrections of AVISO/DUACS Surface Velocities and Its Application to Mesoscale Eddies in the Mediterranean Sea, Journal of Geophysical Research: Oceans, 124, 8913–8932, https://doi.org/10.1029/2019JC015031, 2019.

Jang, E., Kim, Y. J., Im, J., Park, Y.-G., and Sung, T.: Global sea surface salinity via the synergistic use of SMAP satellite and HYCOM data based on machine learning, Remote Sensing of Environment, 273, 112980, https://doi.org/10.1016/j.rse.2022.112980, 2022.

Kafiabad, H. A., Savva, M. A. C., and Vanneste, J.: Diffusion of inertia-gravity waves by geostrophic turbulence, Journal of Fluid Mechanics, 869, R7, https://doi.org/10.1017/jfm.2019.300, 2019.

Kartal, S.: Assessment of the spatiotemporal prediction capabilities of machine learning algorithms on Sea Surface Temperature data: A comprehensive study, Engineering Applications of Artificial Intelligence, 118, 105675, https://doi.org/10.1016/j.engappai.2022.105675, 2023.

Kingma, D. P. and Ba, J. J. C.: Adam: A Method for Stochastic Optimization, abs/1412.6980, 2014.

Kumar, C., Podestá, G., Kilpatrick, K., and Minnett, P.: A machine learning approach to estimating the error in satellite sea surface temperature retrievals, Remote Sensing of Environment, 255, 112227, https://doi.org/10.1016/j.rse.2020.112227, 2021.
Kwak, Y. S. and Richmond, A. D.: Dependence of the high-latitude lower thermospheric wind vertical vorticity and horizontal divergence on the interplanetary magnetic field, Journal of Geophysical Research: Space Physics, 119, 1356–1368, https://doi.org/10.1002/2013JA019589, 2014.
Lenain, L., Srinivasan, K., Barkan, R., and Pizzo, N.: An unprecedented view of ocean currents from geostationary satellites, Nature Geoscience, 10.1038/s41561-026-01943-0, 2026.
Li, X., Liu, B., Zheng, G., Ren, Y., Zhang, S., Liu, Y., Gao, L., Liu, Y., Zhang, B., and Wang, F.: Deep-learning-based information mining from ocean remote-sensing imagery, National Science Review, 7, 1584–1605, https://doi.org/10.1093/nsr/nwaa047, 2020.
Li, Z., Cai, Z., Liu, Z., Wang, X., and Hu, J.: A novel identification method for unrevealed mesoscale eddies with transient and weak features-Capricorn Eddies as an example, Remote Sensing of Environment, 274, 112981, https://doi.org/10.1016/j.rse.2022.112981, 2022.
Liu, Y., He, Q., Zhan, W., Guo, M., Zheng, Y., Shen, X., and Zhan, H.: Heterogeneity of phytoplankton response to submesoscale processes in the global ocean, Communications Earth & Environment, 6, 386, https://doi.org/10.1038/s43247-025-02365-3, 2025.
Manucharyan, G. E., Siegelman, L., and Klein, P.: A Deep Learning Approach to Spatiotemporal Sea Surface Height Interpolation and Estimation of Deep Currents in Geostrophic Ocean Turbulence, Journal of Advances in Modeling Earth Systems, 13, e2019MS001965, https://doi.org/10.1029/2019MS001965, 2021.
Masuda, Y., Yamanaka, Y., Smith, S. L., Hirata, T., Nakano, H., Oka, A., and Sumata, H.: Photoacclimation by phytoplankton determines the distribution of global subsurface chlorophyll maxima in the ocean, Communications Earth & Environment, 2, 128, https://doi.org/10.1038/s43247-021-00201-y, 2021.
Morales-Márquez, V., Hernández-Carrasco, I., Fox-Kemper, B., and Orfila, A.: Ageostrophic Contribution by the Wind and Waves Induced Flow to the Lateral Stirring in the Mediterranean Sea, Journal of Geophysical Research: Oceans, 128, e2022JC019135, https://doi.org/10.1029/2022JC019135, 2023.
Mulet, S., Rio, M. H., Etienne, H., Artana, C., Cancet, M., Dibarboure, G., Feng, H., Husson, R., Picot, N., Provost, C., and Strub, P. T.: The new CNES-CLS18 global mean dynamic topography, Ocean Science, 17, 789–808, https://doi.org/10.5194/os-17-789-2021, 2021.
Penven, P., Halo, I., Pous, S., and Marié, L.: Cyclogeostrophic balance in the Mozambique Channel, Journal of Geophysical Research: Oceans, 119, 1054–1067, https://doi.org/10.1002/2013JC009528, 2014.
Qin, Y., Su, C., Chu, D., Zhang, J., and Song, J.: A review of application of machine learning in storm surge problems, Journal of Marine Science Engineering, 11, 1729, https://doi.org/10.3390/jmse11091729, 2023.
Qiu, B., Chen, S., Klein, P., Sasaki, H., and Sasai, Y.: Seasonal Mesoscale and Submesoscale Eddy Variability along the North Pacific Subtropical Countercurrent, Journal of Physical Oceanography, 44, 3079–3098, https://doi.org/10.1175/JPO-D-14-0071.1, 2014.
Qiu, C., Mao, H., Wang, Y., Yu, J., Su, D., and Lian, S.: An irregularly shaped warm eddy observed by Chinese underwater gliders, Journal of oceanography, 75, 139–148, https://doi.org/10.1007/s10872-018-0490-0, 2019.
Razavi, M., Mavaddati, S., and Koohi, H.: ResNet deep models and transfer learning technique for classification and quality detection of rice cultivars, Expert Systems with Applications, 247, 123276, https://doi.org/10.1016/j.eswa.2024.123276, 2024.
Rio, M.-H., Mulet, S., and Picot, N.: Beyond GOCE for the ocean circulation estimate: Synergetic use of altimetry, gravimetry, and in situ data provides new insight into geostrophic and Ekman currents, Geophysical Research Letters, 41, 8918–8925, https://doi.org/10.1002/2014GL061773, 2014.
Roquet, F., Bell, M. J., de Boer, A. M., Ferreira, D., Jones, C. S., LaCasce, J. H., de Lavergne, C., Marshall, D. P., Munday, D. R., Nycander, J., and Ödalen, M.: Controls of the global overturning circulation of the ocean, npj Climate and Atmospheric Science, 8, 304, 10.1038/s41612-025-01185-8, 2025.
Ruiz, S., Pelegrí, J. L., Emelianov, M., Pascual, A., and Mason, E.: Geostrophic and ageostrophic circulation of a shallow anticyclonic eddy off Cape Bojador, Journal of Geophysical Research: Oceans, 119, 1257–1270, https://doi.org/10.1002/2013JC009169, 2014.

Shang, J., Shi, H., Yuan, M., Wu, Q., Lv, A., Dou, F., Yin, H., Liu, L., and Hu, X.: Satellite-Ground Integrated External Calibration of the WindRAD Scatterometer Onboard FY-3E Satellite, IEEE Transactions on Geoscience and Remote Sensing, 63, 1–10, https://doi.org/10.1109/TGRS.2025.3526834, 2025.

Shankar, D., Vinayachandran, P. N., and Unnikrishnan, A. S.: The monsoon currents in the north Indian Ocean, Progress in Oceanography, 52, 63–120, https://doi.org/10.1016/S0079-6611(02)00024-1, 2002.

Shchepetkin, A. F. and McWilliams, J. C.: The regional oceanic modeling system (ROMS): a split-explicit, free-surface, topography-following-coordinate oceanic model, Ocean Modelling, 9, 347–404, https://doi.org/10.1016/j.ocemod.2004.08.002, 2005.

Sinha, A. and Abernathey, R.: Estimating Ocean Surface Currents With Machine Learning, Frontiers in Marine Science, 8, https://doi.org/10.3389/fmars.2021.672477, 2021.

Srinivasan, M. and Tsontos, V.: Satellite Altimetry for Ocean and Coastal Applications: A Review, Remote Sensing, 15, https://doi.org/10.3390/rs15163939, 2023.

Su, F., Fan, R., Yan, F., Meadows, M., Lyne, V., Hu, P., Song, X., Zhang, T., Liu, Z., Zhou, C., Pei, T., Yang, X., Du, Y., Wei, Z., Wang, F., Qi, Y., and Chai, F.: Widespread global disparities between modelled and observed mid-depth ocean currents, Nature Communications, 14, 2089, 10.1038/s41467-023-37841-x, 2023.

Sudre, J., Maes, C., and Garçon, V.: On the global estimates of geostrophic and Ekman surface currents, Limnology Oceanography: Fluids Environments, 3, 1–20, https://doi.org/10.1215/21573689-2071927, 2013.

Thomas, J. and Daniel, D.: Forward flux and enhanced dissipation of geostrophic balanced energy, Journal of Fluid Mechanics, 911, A60, https://doi.org/10.1017/jfm.2020.1026, 2021.

Timmermans, M.-L. and Marshall, J.: Understanding Arctic Ocean Circulation: A Review of Ocean Dynamics in a Changing Climate, Journal of Geophysical Research: Oceans, 125, e2018JC014378, https://doi.org/10.1029/2018JC014378, 2020.

Uchida, H. and Imawaki, S.: Eulerian mean surface velocity field derived by combining drifter and satellite altimeter data, Geophys. Res. Lett., 30, https://doi.org/10.1029/2002GL016445, 2003.

Ueno, H., Bracco, A., Barth, J. A., Budyansky, M. V., Hasegawa, D., Itoh, S., Kim, S. Y., Ladd, C., Lin, X., Park, Y.-G., Prants, S., Ross, T., Rypina, I. I., Sasai, Y., Trusenkova, O. O., Ustinova, E. I., and Zhong, Y.: Review of oceanic mesoscale processes in the North Pacific: Physical and biogeochemical impacts, Progress in Oceanography, 212, 102955, https://doi.org/10.1016/j.pocean.2022.102955, 2023.

Van Meurs, P. and Niiler, P. P.: Temporal variability of the large-scale geostrophic surface velocity in the northeast Pacific, Journal of physical oceanography, 27, 2288–2297, https://doi.org/10.1175/1520-0485(1997)027<2288:TVOTLS>2.0.CO;2, 1997.

Wunsch, C.: Patterns of kinetic energy conversion in a time-average upper ocean, Progress in Oceanography, 234, 103453, https://doi.org/10.1016/j.pocean.2025.103453, 2025.

Xie, C., Gao, A.-K., and Lu, X.: Global Estimation of Subsurface Eddy Kinetic Energy of Mesoscale Eddies Using a Multiple-input Residual Neural Network, arXiv, https://doi.org/10.48550/arXiv.2412.10656, 2024.

Zhang, W., Griffies, S. M., Hallberg, R. W., Kuo, Y.-H., and Wolfe, C. L. P.: The Role of Surface Potential Vorticity in the Vertical Structure of Mesoscale Eddies in Wind-Driven Ocean Circulations, Journal of Physical Oceanography, 54, 1243–1266, https://doi.org/10.1175/JPO-D-23-0203.1, 2024.

Zhang, Z., Qiu, B., Klein, P., and Travis, S.: The influence of geostrophic strain on oceanic ageostrophic motion and surface chlorophyll, Nature Communications, 10, 2838, https://doi.org/10.1038/s41467-019-10883-w, 2019.

Zhou, X., Zhu, S., Jia, W., and Yao, H.: Estimating Subsurface Thermohaline Structure in the Tropical Western Pacific Using DO-ResNet Model, Atmosphere, 15, https://doi.org/10.3390/atmos15091043, 2024.

Supplementary Materials

Daily Global Sea Surface Ageostrophic Current Dataset from 1993–2023 via Physics-Informed Deep Learning

Guangxi Cui[1,2], Ka-Veng Yuen[3], Ying Chen[1,2], Zhiqiang Liu[4], Dingqi Yang[5], Guanliang Liu[6,7], Zhongya Cai[1,2*]

[1]State Key Laboratory of Internet of Things for Smart City, Department of Ocean Science and Technology, University of Macau

[2]Center for Ocean Research in Hong Kong and Macau (CORE), Hong Kong

[3]State Key Laboratory of Internet of Things for Smart City, Department of Civil and Environmental Engineering, University of Macau

[4]Department of Ocean Science and Engineering and Center for Complex Flows and Soft Matter Research, Southern University of Science and Technology, Shenzhen, China

[5]State Key Laboratory of Internet of Things for Smart City, Department of Computer and Information Science, University of Macau

[6]State Key Laboratory of Physical Oceanography, Institute of Oceanographic Instrumentation, Shandong Academy of Sciences

[7]Qilu University of Technology (Shandong Academy of Sciences), Jinan

Table S1. Hyperparameters and training configurations of the AC-PIDNN model.

Category	Hyperparameter / Setting	Value / Description
Network Configuration	Optimizer	Adam
	Weight Initialization	Xavier
	Activation Function	Tanh
Regularization (to prevent overfitting)	Dropout Rate	0.3
	L2 Regularization Factor (λ)	0.01
Stage 1: Initialization (Quickly fit geostrophic current)	Loss Function	$Loss_{data}$
	Learning Rate	0.001
	Epochs	1000
Stage 2: Transition (Gradually introduce physical constraints)	Loss Function	$Loss_{hybrid}$
	Hybrid Loss Proportion	1:1
	Learning Rate	0.0001
	Epochs	1000
Stage 3: Physics-Informed (Minimize momentum equation residuals)	Loss Function	$Loss_{physics}$
	Learning Rate	0.00001
	Epochs	10000

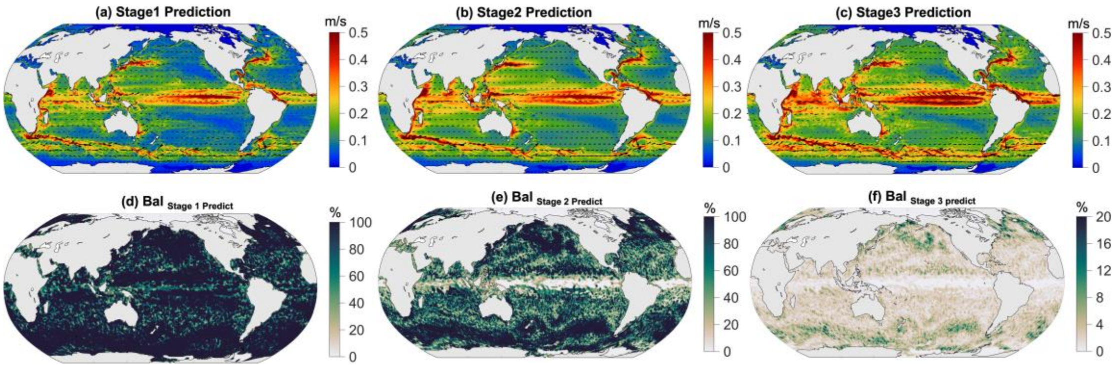

Figure S1. (a) Mean output current field of AC-PIDNN Stage 1 in 2021; (b) Mean output current field of AC-PIDNN Stage 2 in 2021; (c) Final mean output current field of AC-PIDNN Stage 3 in 2021; (d) Momentum balance (Bal) results for Stage 1; (e) Momentum balance (Bal) results for Stage 2; (f) Momentum balance (Bal) results for Stage 3.

To quantify the precise contribution of the physics-informed loss function within the neural network's training pipeline, a dedicated ablation study was conducted utilizing global flow field data from the year 2021. This experiment isolated the different loss constraints to evaluate their impact on both dynamical consistency and observational accuracy. The model was re-trained using the 2021 dataset, and the daily predicted surface currents were extracted across three distinct training phases: Stage 1 (representing the data-loss-only baseline), Stage 2 (hybrid loss optimization), and Stage 3 (the fully physics-constrained final model). By comparing these intermediate outputs against both theoretical momentum balance metrics (Bal) and station-based observational errors, the value added by the physical constraints beyond pure data-driven mapping can be systematically delineated.

A primary objective of integrating a Physics-Informed Neural Network (PINN) architecture is to ensure that the reconstructed ocean surface currents adhere to the governing physical laws of ocean dynamics, rather than merely minimizing the statistical error against remote sensing observations. As illustrated in Figures S1(a)–(c), the annual mean surface current fields generated by the AC-PIDNN model during Stages 1, 2, and 3 exhibit a stark contrast in dynamical consistency when evaluated alongside their corresponding momentum balance residuals (Figures S1(d)–(f)). Because the initial Stage 1 relies exclusively on data loss without any embedded physical constraints, the neural network acts as a standard data-fitting algorithm. Consequently, the output entirely lacks momentum balance correction, leading to severe dynamical inconsistencies where the momentum residuals exceed 100% across the vast majority of the global ocean regions. Upon introducing a hybridized loss function in Stage 2 that begins blending physical constraints with observational data, a dramatic correction in the flow field's dynamical structure is observed, with the global mean momentum residual dropping precipitously to approximately 51%. In the final Stage 3, the output is rigorously constrained by the complete physics loss. This proper parameterization forces the reconstructed flow field to obey the fundamental equations of motion, vastly improving the momentum balance and reducing the global average momentum residual to a mere 1.2%. This progression unequivocally demonstrates that the physics-informed stages provide a profound improvement extending well beyond initial data fitting. The physics loss serves as a critical mechanism that enforces strict physical consistency, thereby ensuring the hydrodynamic reliability of the reconstructed surface currents.

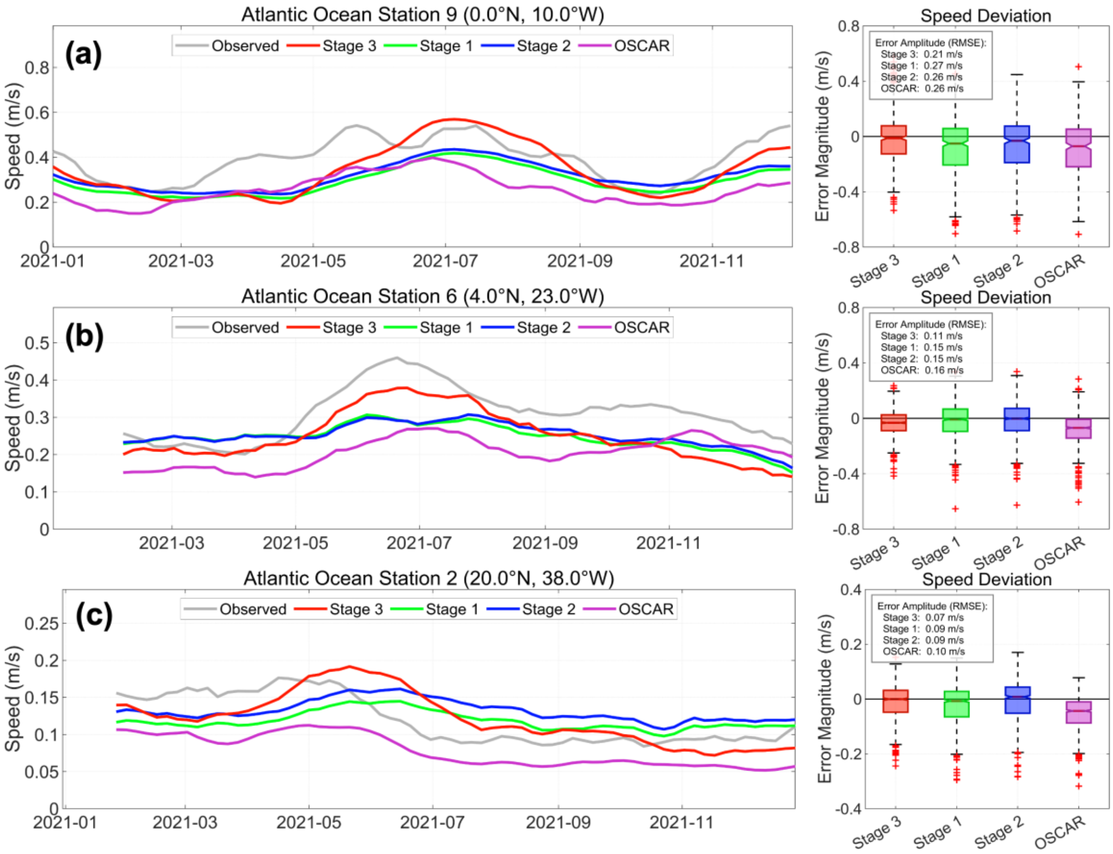

Figure S2. Comparison of the output current fields from the three training stages of AC-PIDNN and OSCAR product velocities against in-situ observational data.

To confirm that this improved dynamical balance translates to real-world accuracy, the outputs of all three training stages, alongside the standard OSCAR product, were further evaluated against independent in-situ mooring data. Focusing on the velocity time series from successfully matched observation stations in 2021, the progressive incorporation of physical laws was shown to systematically refine the accuracy of the modeled velocities. The average errors were recorded as 0.17 m/s for Stage 1, 0.16 m/s for Stage 2, and 0.13 m/s for Stage 3, compared to 0.17 m/s for the OSCAR product. The data clearly indicate that the Stage 3 output aligns most closely with the in-situ measurements, significantly outperforming the Stage 1 baseline, the intermediate Stage 2 output, and the widely used OSCAR product. Purely data-driven approaches (Stage 1) remain highly susceptible to the inherent noise and spatial gaps present in multi-source satellite altimetry and scatterometry data. By enforcing momentum conservation, the subsequent physics-informed stages effectively filter out dynamically impossible artifacts, preventing overfitting to observational noise and yielding a flow field that is both physically coherent and statistically more accurate. This direct comparison firmly substantiates the superiority and absolute necessity of the physics-informed training stages within the AC-PIDNN framework.

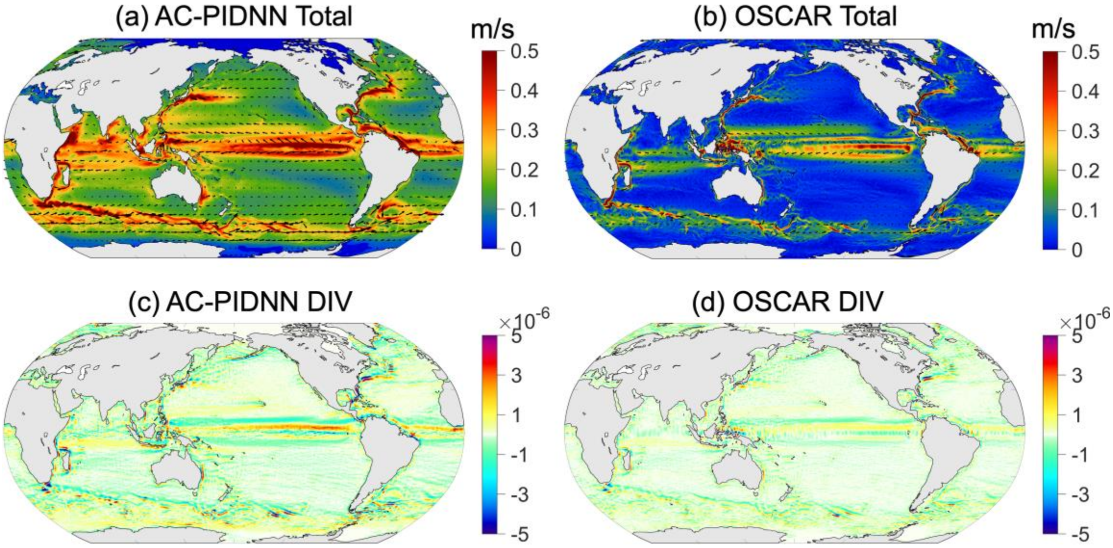

Figure S3. (a) 1993–2022 mean flow field from AC-PIDNN; (b) 1993–2022 mean flow field from the OSCAR product; (c) divergence of the 1993–2022 mean flow field from AC-PIDNN; (d) divergence of the 1993–2022 mean flow field from the OSCAR product.

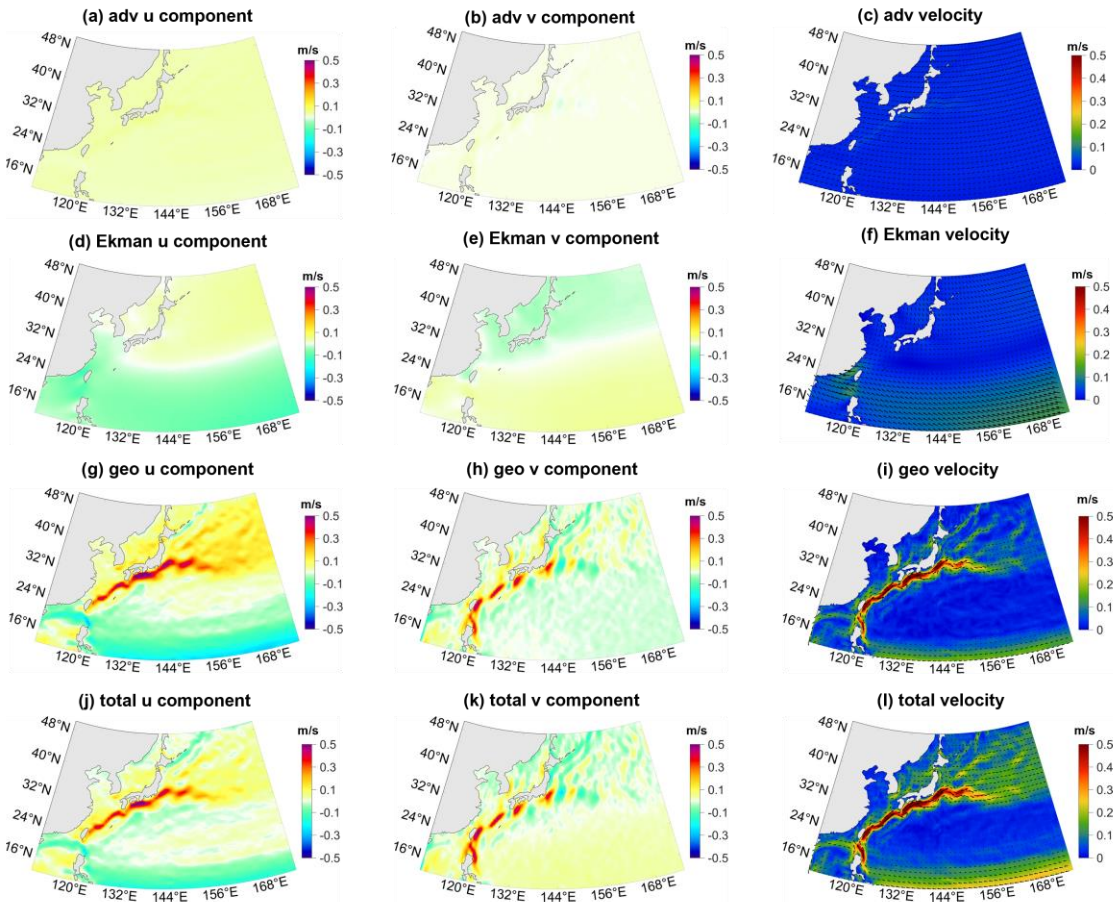

Figure S4: Results of sea surface circulation correction for the Kuroshio Current from 1993 to 2023, using the AC-PIDNN model. Panels (a)–(c) show the u-component, v-component, and flow field of the advective component; panels (d)–(f) show the u-component, v-component, and flow field of the Ekman component; panels (g)–(i) show the u-component, v-component, and flow field of the geostrophic component; panels (j)–(l) show the u-component, v-component, and flow field of the total circulation.

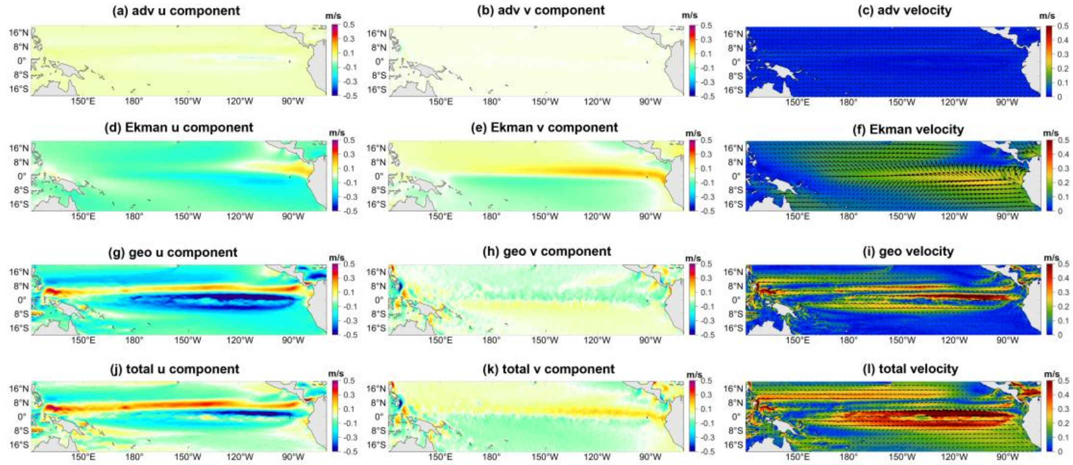

Figure S5: Results of sea surface circulation correction for the Equatorial Region from 1993 to 2023, using the AC-PIDNN model. Panels (a)–(c) show the u-component, v-component, and flow field of the advective component; panels (d)–(f) show the u-component, v-component, and flow field of the Ekman component; panels (g)–(i) show the u-component, v-component, and flow field of the geostrophic component; panels (j)–(l) show the u-component, v-component, and flow field of the total circulation.

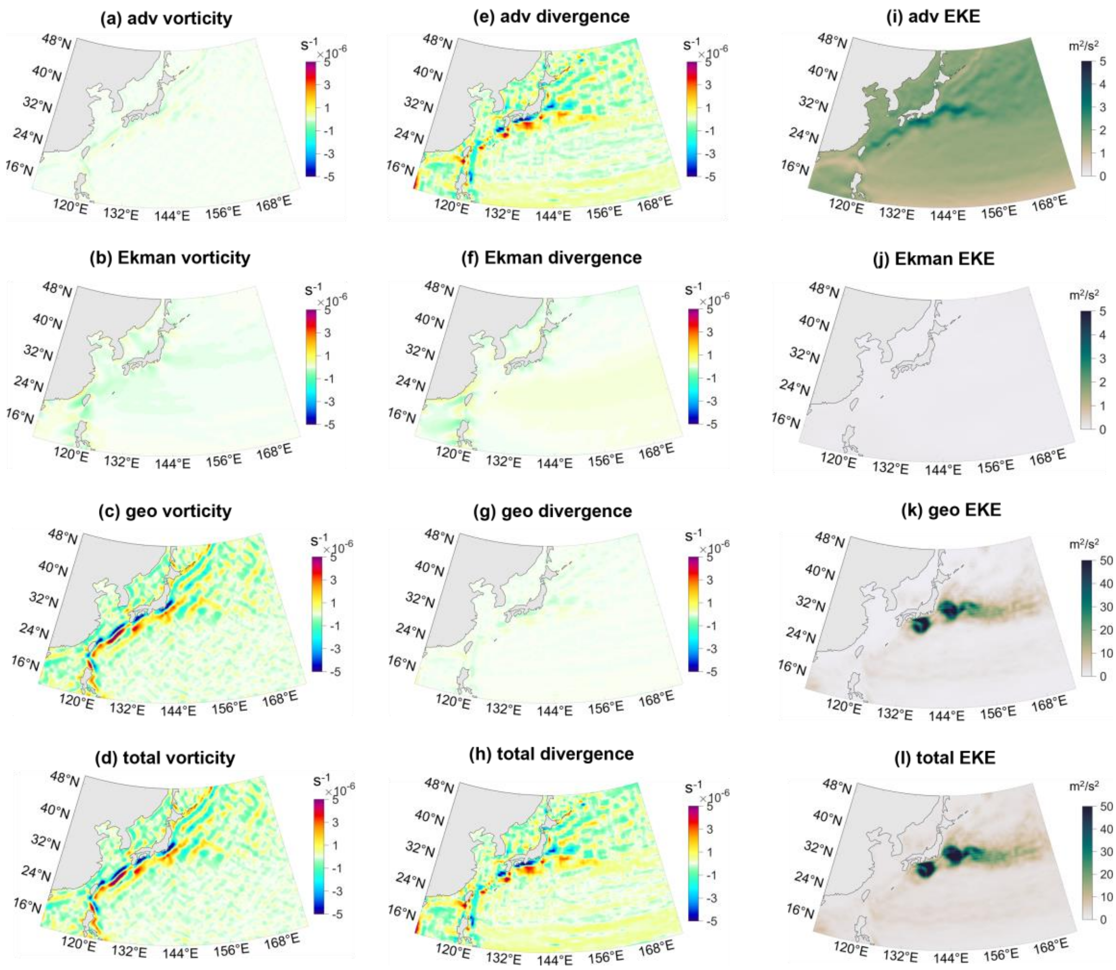

Figure S6: Characteristics of the dynamic parameters of the corrected 30-year average sea surface circulation in the Kuroshio Current. Panels (a)–(d) showing the vorticity of the advective, Ekman, geostrophic, and total components, respectively; panels (e)–(h) showing the divergence of the advective, Ekman, geostrophic, and total components, respectively; panels (i)–(l) showing the eddy kinetic energy (EKE) of the advective, Ekman, geostrophic, and total components, respectively.

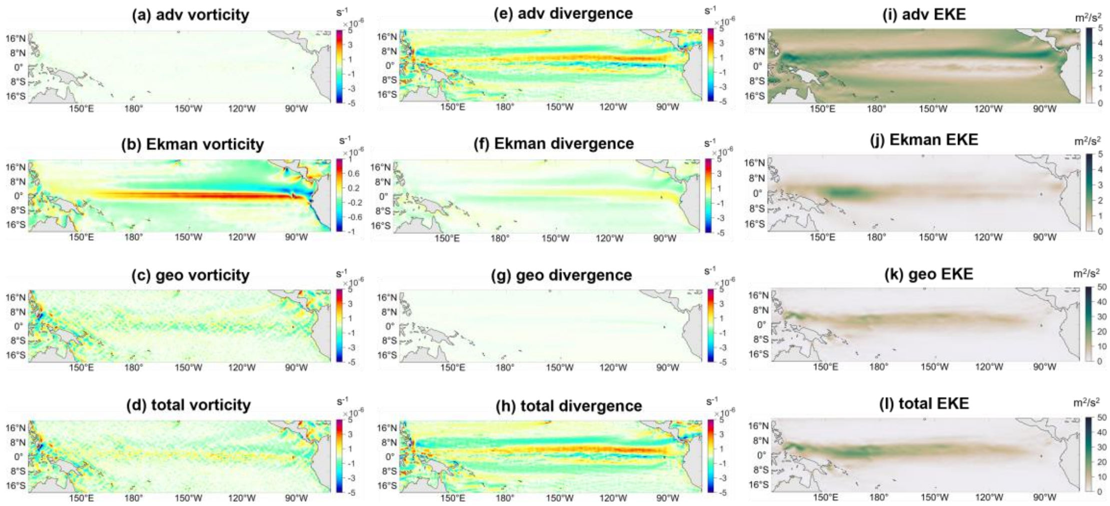

Figure S7: Characteristics of the dynamic parameters of the corrected 30-year average sea surface circulation in the Equatorial Region. Panels (a)–(d) showing the vorticity of the advective, Ekman, geostrophic, and total components, respectively; panels (e)–(h) showing the divergence of the advective, Ekman, geostrophic, and total components, respectively; panels (i)–(l) showing the eddy kinetic energy (EKE) of the advective, Ekman, geostrophic, and total components, respectively.